ACS OMEGA

http://pubs.acs.org/journal/acsodf

Article

Osmium Arene Germyl, Stannyl, Germanate, and Stannate Complexes as Anticancer Agents

Tomiris Nabiyeva,[‖] Basile Roufosse,[‖] Matylda Odachowski, Judith Baumgartner, Christoph Marschner, Akalesh Kumar Verma,* and Burgert Blom*

Cite This: *ACS Omega* 2021, 6, 19252−19268

Read Online

ACCESS | Metrics & More | Article Recommendations | Supporting Information

ABSTRACT: Herein, we describe the synthesis, full spectroscopic characterization, DFT (density functional theory) calculations, and single-crystal X-ray diffraction analyses of a series of osmium arene σ-germyl, germanate, σ-stannyl, and stannate complexes, along with their cytotoxic (anticancer) investigations. The known dimer complexes $[OsCl_2(\eta^6\text{-}C_6H_6)]_2$ (**1**) and $[OsCl_2(\eta^6\text{-}p\text{-cymene})]_2$ (**2**) were reacted with PPh_3 to form the known mononuclear complex $[OsCl_2(\eta^6\text{-}p\text{-cymene})(PPh_3)]$ (**3**) and the new complex $[OsCl_2(\eta^6\text{-}C_6H_6)(PPh_3)]$ (**6**); complex **3** was reacted with $GeCl_2\cdot$(dioxane) and $SnCl_2$ to afford, by insertion into the Os−Cl bond, the neutral σ-germyl and stannyl complexes $[OsCl(\eta^6\text{-}p\text{-cymene})(PPh_3)(GeCl_3)]$ (**7**) and $[OsCl(\eta^6\text{-}p\text{-cymene})(PPh_3)(SnCl_3)]$ (**11**), respectively, as a mixture of enantiomers. Similarly, the reaction of complex **6** with $GeCl_2\cdot$(dioxane) afforded $[OsCl(\eta^6\text{-}C_6H_6)(PPh_3)(GeCl_3)]$ (**9**). Complex **2**, upon reaction with 1,1-bis(diphenylphosphino)methane (dppm), formed a mixture of $[OsCl_2(\eta^6\text{-}p\text{-cymene})(\kappa^1\text{-dppm})]$ (**4**) and $[Os(\eta^6\text{-}p\text{-cymene})(\kappa^2\text{-dppm})Cl]^+Cl^-$ (**5**) when prepared in acetonitrile and a mixture of **4** and the dinuclear complex $[[OsCl_2(\eta^6\text{-}p\text{-cymene})]_2(\mu\text{-dppm})]$ (**0**) when prepared in dichloromethane. By utilizing either isolated **4** or a mixture of **4** and **5**, the synthesis of κ^2-dppm germanate and stannate salts, $[OsCl(\eta^6\text{-}p\text{-cymene})(\kappa^2\text{-dppm})]^+GeCl_3^-$ (**8**) and $[OsCl(\eta^6\text{-}p\text{-cymene})(\kappa^2\text{-dppm})]^+SnCl_3^-$ (**10**), were accomplished *via* halide-abstracting reactions with $GeCl_2\cdot$(dioxane) or $SnCl_2$, respectively. All resulting complexes were characterized by means of multinuclear NMR, FT-IR, ESI-MS, and UV/Vis spectroscopy. X-ray diffraction analyses of **4**, **8**, **9**, **10**, and **11** were performed and are reported. DFT studies (B3LYP, basis set LANL2DZ for Os, and def2-TZVPP for Sn, Ge, Cl, P, C, and H) were performed on complex **9** and the benzene analogue of complex **11**, **11−benzene**, to evaluate the structural changes and the effects on the frontier molecular orbitals arising from the substitution of Ge for Sn. Finally, complexes **3** and **7−11** were investigated for potential anticancer activities considering cell cytotoxicity and apoptosis assays against Dalton's lymphoma (DL) and Ehrlich ascites carcinoma (EAC) malignant cancer cell lines. The complexes were also tested against healthy peripheral blood mononuclear cells (PBMCs). All cell lines were also treated with the reference drug cisplatin to draw a comparison with the results obtained from the reported complexes. The study was further corroborated with *in silico* molecular interaction simulations and a pharmacokinetic study.

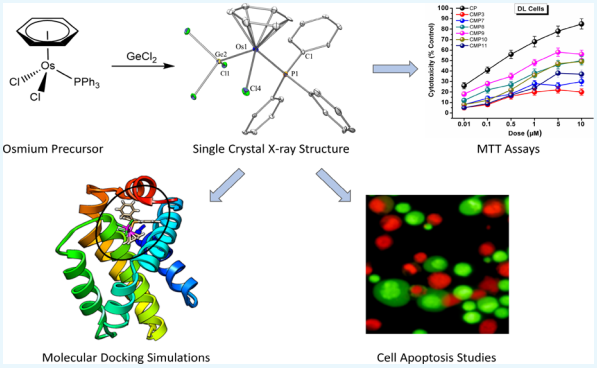

1. INTRODUCTION

Despite the continuous decline in cancer death rates in recent years, cancer remains one of the leading causes of death worldwide.[1] Chemotherapy remains the principal form of cancer treatment,[2] and in recent years, much research has focused on the development of targeted therapies that bypass the off-target toxic side effects of chemotherapy.[3] However, such therapies are often reliant on targetable pheno- and genotypes. As such, chemotherapy remains a reliable form of treatment for tumors that do not display such specific targets.[4]

Traditionally, platinum-based drugs occupy a prominent role in anticancer treatment[5] but causes severe side effects.[6] Additionally, an acquired resistance to platinum-based agents displayed by many tumors further limits their use in clinical practice.[7] These drawbacks have led to the pursuit of nonplatinum metal complexes that display superior anticancer activity while potentially minimizing the negative side effects associated with platinum agents.[8] Among these, ruthenium,[9] iridium,[10] gold,[11] and osmium[12] compounds have been established as potential candidates in the past 20 years, with

Received: May 24, 2021
Accepted: June 29, 2021
Published: July 12, 2021

ruthenium complexes being the most well studied and showing promise in a number of clinical trials.

We have reported a series of neutral ruthenium-based germyl ([Ru]−$GeCl_3$) and stannyl ([Ru]−$SnCl_3$) complexes that displayed less than optimal cytotoxic activity on numerous cell lines *in vitro* (Scheme 1).[13,15] In contrast, ruthenium

Scheme 1. Several Previously Reported Ruthenium-Based Germyl, Stannyl, Germanate, and Stannate Complexes,[13a,14,15]

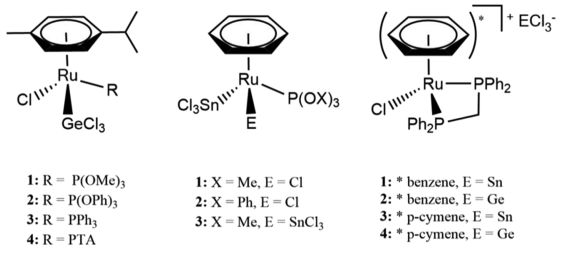

1: R = $P(OMe)_3$
2: R = $P(OPh)_3$
3: R = PPh_3
4: R = PTA

1: X = Me, E = Cl
2: X = Ph, E = Cl
3: X = Me, E = $SnCl_3$

1: * benzene, E = Sn
2: * benzene, E = Ge
3: * p-cymene, E = Sn
4: * p-cymene, E = Ge

germanate and stannate salt complexes displayed potent and promising cytotoxic activity on two breast cancer cell lines (MCF-7 and MDA-MB-231) and good selectivity, suggesting that the ionic nature of the complexes influences their biological effects.[14]

Osmium, as a heavier analogue of ruthenium, might be expected to be a suitable metal for anticancer applications; however, when compared to ruthenium, research into osmium-based anticancer agents is less pronounced. Osmium is the least abundant metal on Earth, which might limit its application with regard to widespread use in clinical applications. Nevertheless, in contrast to ruthenium, osmium complexes exhibit some different characteristics: slow ligand exchange kinetics,[16] predilection for higher oxidation states, elevated levels of inertness,[2b] and stronger π-backdonation when in low oxidation states.[17] Many osmium complexes have been synthesized and tested as potential anticancer agents,[12a,18] which in comparison to analogous ruthenium compounds suggest that osmium as a metal center may be beneficial.[12e−g] Other osmium arene complexes have shown high cytotoxicity, although their mechanism implied DNA unwinding rather than bending.[19] Depending on the structure and the oxidation state of the osmium metal in numerous complexes, varied mechanisms of action have been observed. For example, synthesized octahedral complexes **a** and **b** (Scheme 2) both induced cellular apoptosis: **b** by inducing endoplasmic reticulum stress and enlargement as well as upregulation of protein p53, whereas **a** by interrupting the replication cycle at the G2/M stage.[12a] Most importantly, **a** exhibited activity against cancer stem cells that are responsible

Scheme 2. Selected Examples of Osmium-Based Anticancer Agents,[12a,20]

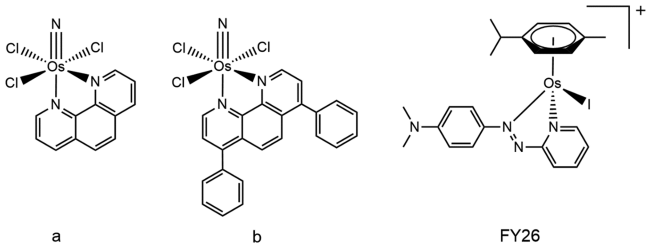

a b FY26

for cancer recurrence.[12a] Another osmium complex, FY26 (Scheme 2), inhibits tumor growth by increasing the production of reactive oxygen species (ROS) inside the targeted cells.[20]

Several recent reviews have been devoted to the potential of osmium anticancer agents.[2b,17,19b] We have also recently reviewed all existing osmium complexes mutually bearing π-bound arene groups and a phosphane coligand in a biological context.[12a] Inspired by our earlier work on ruthenium-based stannyl/stannate and germyl/germanate complexes, we envisaged an extension of that work to osmium. Surprisingly, osmium arene complexes bearing σ-bound germyl or stannyl ligands are exceptionally rare in the literature: only two reports by Wen *et al.*[21] and Albertin *et al.*[22] exist. No osmium-based germanate or stannate complexes have been reported in the literature to this date to the best of our knowledge. The anticancer or biological activity investigations of any of these four classes of compounds or elucidations of their bonding nature by theoretical methods have not previously been evaluated. Moreover, given our previous numerous studies on ruthenium arene stannyl and stannate complexes, as well as their germanium analogues,[13a,14,15] the extension to osmium is expected to yield different biological activities given the rather inert nature of Os(II) vs Ru(II) (see above). This hence motivated us to explore the analogous osmium chemistry with a view of biological anticancer applications, not as a mere extension from Ru, but expecting different *in vitro* biological activities compared to analogous ruthenium complexes.

Herein, we describe the synthesis and full spectroscopic characterization of rare examples of osmium arene-based germyl and stannyl complexes and the first germanate and stannate complexes of osmium. We also report the *in vitro* activities of the complexes against Dalton's lymphoma (DL) and Ehrlich ascites carcinoma (EAC) malignant cancer cell lines as well as healthy peripheral blood mononuclear cells (PBMCs) using MTT and apoptosis assays. Furthermore, an *in silico* molecular interaction study and pharmacokinetic tests were also performed to support the results.

2. MATERIALS AND METHODS

2.1. General Considerations. All reactions were conducted under a nitrogen atmosphere using standard glovebox and Schlenk techniques, unless otherwise stated. Chemicals used were obtained from commercial sources and used as received. $OsCl_3{\cdot}xH_2O$ was purchased from Strem Chemicals. 1,3-Cyclohexadiene, α-terpinene (85%), triphenylphosphine (PPh_3), and bis(diphenylphosphino)methane (97%) (dppm) were purchased from Sigma-Aldrich. Reagent-grade diethyl ether (stab. BHT) and dichloromethane (stab. amylene) were purchased from Biosolve Chimie SARL. $[OsCl_2(\eta^6\text{-}C_6H_6)]_2$ (**1**), $[OsCl_2(\eta^6\text{-}p\text{-cymene})]_2$ (**2**), and $[OsCl_2(\eta^6\text{-}p\text{-cymene})(PPh_3)]$ (**3**) were synthesized according to literature methods.[23] All solvents were purged with nitrogen prior to use. The NMR data were acquired on a 300 MHz Ultrashield Magnet System (Bruker). The NMR samples were prepared in deuterated chloroform ($CDCl_3$), unless otherwise stated. Chemical shifts of $^{31}P\{^1H\}$ NMR peaks were reported relative to phosphoric acid (85%), and ^1H and $^{13}C\{^1H\}$ NMR resonance signals were measured relative to tetramethylsilane (TMS) and were reported in parts per million. Abbreviations: s = singlet; d = doublet; t = triplet; dd = doublet of doublets; dt = doublet of triplets; pst = pseudo triplet; m = multiplet; sept = septet. NMR data were processed using TopSpin 4.0.8

https://doi.org/10.1021/acsomega.1c02665
ACS Omega 2021, 6, 19252−19268

software or MestReNova. Infrared spectroscopy was performed on a Shimadzu MIRacle 10 spectrometer (Shimadzu single reflexion ATR accessory). The analysis was performed with the following settings: 128 scans; resolution, 2; Happ−Genzel apodization. Abbreviations: v = variable; w = weak; m = medium; s = strong; br = broad. The IR spectra were processed using IR solution software. The UV/Vis absorption spectra were recorded with a Shimadzu UV-1800 spectrophotometer using 1 cm path length quartz cuvettes with a reference cell containing dichloromethane, and the maximum absorption peak(s) were reported. Melting points were measured in glass capillary tubes on a Stuart BioCote SMP10 machine and performed in triplicate. An average of the measurements was reported in degrees Celsius and was uncorrected. A direct injection method was utilized for EI-MS measurements performed on a GCMS-QP2010 Ultra (Shimadzu). For the high-resolution ESI-MS measurements, the samples were sent either to Technische Universität Berlin where the data were acquired with an Orbitrap LTQ XL mass spectrometer (Thermo Scientific) or to Maastricht MultiModal Molecular Imaging Institute (M4I) where the results were acquired on a Bruker SolariX XR FT-ICR-MS. The signals for both EI-MS and ESI-MS were thoroughly checked and compared to the theoretical isotope patterns predicted by online software enviPat Web 2.4.[24] The peaks with the highest intensity from the corresponding isotope pattern were reported. Crystals suitable for X-ray diffraction analysis were analyzed at TU Graz, Austria, on a BRUKER-AXS SMART APEX CCD diffractometer using graphite-monochromated Mo Kα radiation (0.71073 Å).

2.2. Synthesis of a Separable Mixture of [$OsCl_2$(η^6-*p*-cymene)(κ^1-dppm)] (4) and [OsCl(η^6-*p*-cymene)(κ^2-dppm)]$^+Cl^-$ (5). A total of 185 mg (0.481 mmol, 2 equiv) of dppm was reacted with 190.2 mg (0.241 mmol) of **2** in 30 mL of acetonitrile. The solution was refluxed under nitrogen for 1.5 h. The resulting orange solution was filtered and washed with acetonitrile; the solvent was then evaporated *in vacuo*. The resulting translucent yellow oil was washed with diethyl ether (3 × 10 mL), which was subsequently evaporated using a rotary evaporator. At this point, $^{31}P\{^1H\}$ NMR spectroscopy revealed the presence of two products: the desired **4** and another complex [Os(η^6-*p*-cymene)(κ^2-dppm)-Cl]$^+Cl^-$ (**5**). Thereafter, fractional recrystallization was performed using dichloromethane and diethyl ether. The supernatant was collected *via* decantation. The solvent of this supernatant was then evaporated to dryness, yielding an orange solid. The solvents remaining in the original reaction vessel were removed *in vacuo*, affording a yellow solid. The supernatant fraction was determined to be **4**. Air-stable. 120.8 mg (0.155 mmol) of orange solid (32%). Melting point: 163 °C + dec. ^1H NMR (300 MHz, $CDCl_3$, 298 K): δ 7.85−7.81, 7.33−7.30 and 7.15−7.04 (20H, all m, phenyls, κ^1-dppm), 5.44 (2H, d, $^3J_{H-H}$ = 5.4 Hz, $C^{2,6\text{ or }3,5}H$, η^6-*p*-cymene), 5.32 (2H, d, $^3J_{H-H}$ = 5.6 Hz, $C^{2,6\text{ or }3,5}H$, η^6-*p*-cymene), 3.55 (2H, dd, $^2J_{P^A-H}$ = 8.7 Hz, $^2J_{P^B-H}$ = 1.8 Hz, PCH_2P), 3.48 (0.07 **4**·OEt_2), 2.34 (1H, sept, $^3J_{H-H}$ = 6.9 Hz, $CH(CH_3)_2$), 1.98 (3H, s, CH_3), 1.21 (0.07 **4**·OEt_2), 0.83 (6H, d, $^3J_{H-H}$ = 6.9 Hz, $CH(CH_3)_2$). $^{31}P\{^1H\}$ NMR (121.4 MHz, $CDCl_3$, 298 K): δ −16.1 (d, $^2J_{P-P}$ = 34.9 Hz, Os*P*), −28.8 (d, $^2J_{P-P}$ = 34.9 Hz, CH_2P). FTIR (cm^{-1}): 3055 (w), 2968 (w), 2875 (w), 1481 (vw), 1434 (m), 1374 (w), 1316 (w), 1269 (vw), 1204 (w), 1185 (w), 1155 (w), 1128 (w), 1097 (m), 1027 (w), 999 (w), 900 (w), 874 (vw), 800 (w), 769 (vm), 757 (m), 745 (s), 730 (s), 708 (s), 690 (s), 659 (m). UV/Vis (dichloromethane): λ_{max} = 351 nm. The precipitate of the original reaction vessel was determined to be [OsCl(η^6-*p*-cymene)(κ^2-dppm)]$^+Cl^-$ (**5**). Air-stable. 154.0 mg (0.198 mmol) of yellow solid (41%). Melting point: 176 °C + dec. ^1H NMR (300 MHz, $CDCl_3$, 298 K): δ 7.61−7.46 (20H, m, phenyls, κ^2-dppm), 6.47 (1H, dt, $^2J_{H-H}$ = 15.3 Hz, $^2J_{H-P}$ = 9.8 Hz, $PCH^{A\text{ or }B}P$), 6.29 (4H, d, $^3J_{H-H}$ = 37.3 Hz, $C^{3,5\text{ and }2,6}H$, η^6-*p*-cymene), 3.48 (0.33 **5**·OEt_2), 4.70 (1H, dt, $^2J_{H-H}$ = 15.1 Hz, $^2J_{H-P}$ = 12.8 Hz, $PCH^{A\text{ or }B}P$), 2.41 (1H, sept, $^3J_{H-H}$ = 6.9 Hz, $CH(CH_3)_2$), 1.67 (3H, s, CH_3), 1.21 (0.33 **5**·OEt_2), 1.09 (6H, d, $^3J_{H-H}$ = 6.9 Hz, $CH(CH_3)_2$). $^{13}C\{^1H\}$ NMR (75.4 MHz, $CDCl_3$, 298 K): δ 132.2 (pst, *J* = 5.0 Hz, κ^2-dppm), 131.8 (pst, *J* = 5.0 Hz, κ^2-dppm), 129.6 (pst, *J* = 5.5 Hz, κ^2-dppm), 128.8 (pst, *J* = 5.5 Hz, κ^2-dppm), 128.1 (s, C^4H,κ^2-dppm), 114.9 (s, $C^{1\text{ or }4}$, η^6-*p*-cymene), 95.2 (s, $C^{1\text{ or }4}$, η^6-*p*-cymene), 84.3 (s, $C^{2,6\text{ or }3,5}H$, η^6-*p*-cymene), 82.2 (t, $^2J_{C-P}$ = 3.7 Hz, $C^{2,6\text{ or }3,5}H$, η^6-*p*-cymene), 65.9 (**5**·OEt_2), 46.1 (t, $^1J_{C-P}$ = 32.3 Hz, PCH_2P), 30.5 (s, $CH(CH_3)_2$), 22.1 (s, $CH(CH_3)_2$), 17.2 (s, CCH_3), 15.3 (**5**·OEt_2). $^{31}P\{^1H\}$ NMR (121.4 MHz, $CDCl_3$, 298 K): δ −40.0 (s).

2.3. Synthesis of a Mixture of [$OsCl_2$(η^6-*p*-cymene)(κ^1-dppm)] (4) and [OsCl(η^6-*p*-cymene)(κ^2-dppm)]$^+Cl^-$ (5). The reaction was performed in 30 mL of degassed acetonitrile. A total of 146.5 mg (0.185 mmol, 1 equiv) of **2** was dissolved and refluxed with 143.4 mg (0.373 mmol, 2 equiv) of dppm for 1.5 h under nitrogen. After the reaction was complete, the solution was filtered and the solvent was removed *in vacuo*. The crude product was then washed with diethyl ether (3 × 10 mL), the washings were discarded, and the residue was dried *in vacuo*, yielding 228.7 mg (0.293 mmol) of a mixture of **4** and **5**. This mixture was subsequently used for the reactions with germanium(II) chloride·dioxane and with tin(II) chloride to yield **8** and **10**, respectively. Air-stable. All the spectral information was identical to those retrieved from the separated products **4** and **5** (see above).

2.4. Synthesis of a Mixture of [$OsCl_2$(η^6-*p*-cymene)(κ^1-dppm)] (4) and [[$OsCl_2$(η^6-*p*-cymene)]$_2$(μ-bis-(diphenylphosphino)methane)] (0). First, 121.2 mg (0.153 mmol, 1 equiv) of dimer **2** was dissolved in 30 mL of degassed dichloromethane. Then, 118.0 mg (0.307 mmol, 2 equiv) of dppm was added to the flask and the solution was refluxed under nitrogen for 1.5 h. The resultant golden solution was filtered and the solvent was removed *in vacuo*. The obtained oily product was then washed with diethyl ether (3 × 10 mL), and the residue was dried *in vacuo*. A total of 133.9 mg of a mixture of two products was isolated: **4**: ^1H NMR (300 MHz, $CDCl_3$, 298 K): δ 7.87−7.80 (4H, m, $C^{2,6}H$ of $OsP(C_6H_5)_2$ or $CH_2P(C_6H_5)_2$, dppm), 7.33−7.28 (6H, m, $C^{3-5}H$ of $OsP(C_6H_5)_2$ or $CH_2P(C_6H_5)_2$, dppm), 7.14−7.10 (10H, m, $OsP(C_6H_5)_2$ or $CH_2P(C_6H_5)_2$, dppm),5.44 (2H, d, $^3J_{H-H}$ = 5.6 Hz, $C^{2,6\text{ or }3,5}H$, η^6-*p*-cymene), 5.32 (2H, d, $^3J_{H-H}$ = 5.6 Hz, $C^{2,6\text{ or }3,5}H$, η^6-*p*-cymene), 3.55 (2H, dd, $^2J_{P^A-H}$ = 8.9 Hz, $^2J_{P^B-H}$ = 1.8 Hz, PCH_2P), 2.41 (1H, sept, $^3J_{H-H}$ = 6.9 Hz, $CH(CH_3)_2$), 1.98 (3H, s, CCH_3), 0.83 (6H, d, $^3J_{H-H}$ = 6.9 Hz, $CH(CH_3)_2$). $^{13}C\{^1H\}$ NMR (75.4 MHz, $CDCl_3$, 298 K): *i* 137.3 (dd, $^1J_{C-P^A}$ = 14.1 Hz, $^3J_{C-P^B}$ = 5.7 Hz, $C^1P^{A\text{ or }B}$, dppm), 132.5 (dd, $^1J_{C-P^A}$ = 8.8 Hz, $^3J_{C-P^B}$ = 2.3 Hz, $C^1P^{A\text{ or }B}$, dppm), 131.7 (s, C^4H, $P^{A\text{ or }B}$, dppm), 131.4 (s, C^4H, $P^{A\text{ or }B}$, dppm), 129.7 (d, $^YJ_{C-P}$ = 2.0 Hz, $C^{3,5\text{ or }2,6}H$, dppm), 127.5−126.7 (m, $C^{2,6\text{ or }3,5}H$, dppm (overlapping with signals from **0**)), 97.6 (s, $C^{1\text{ or }4}$, η^6-*p*-cymene), 85.2 (s, $C^{1\text{ or }4}$, η^6-*p*-cymene), 81.0 (d, $^2J_{C-P}$ = 4.0 Hz, $C^{2,6\text{ or }3,5}H$, η^6-*p*-cymene),

https://doi.org/10.1021/acsomega.1c02665
ACS Omega 2021, 6, 19252−19268

77.1 (d, $^{2}J_{C-P}$ = 5.2 Hz, $C^{2,6\text{ or }3,5}$H, η^6-*p*-cymene), 28.7 (s, $CH(CH_3)_2$), 20.6 (s, $CH(CH_3)_2$), 17.9 (t, $^{1}J_{C-P}$ = 31.0 Hz, PCH_2P), 16.2 (s, CCH_3). $^{31}P\{^{1}H\}$ NMR (121.4 MHz, $CDCl_3$, 298 K): δ −16.1 (d, $^{2}J_{P-P}$ = 34.9 Hz, Os*P*), −28.8 (d, $^{2}J_{P-P}$ = 34.9 Hz, CH_2P). Dinuclear species (**0**): ^{1}H NMR (300 MHz, $CDCl_3$, 298 K): δ 7.57−7.51 (12H, m, $C^{3-5}H$, dppm), 7.20−7.14 (8H, m, $C^{2,6}H$, dppm), 7.03 (4H, d, $^{3}J_{H-H}$ = 5.5 Hz, $C^{2,6\text{ or }3,5}H$, η^6-*p*-cymene), 5.13 (4H, d, $^{3}J_{H-H}$ = 5.5 Hz, $C^{2,6\text{ or }3,5}H$, η^6-*p*-cymene), 4.68 (2H, t, $^{2}J_{H-P}$ = 7.6 Hz, PCH_2P), 2.32 (2H, sept, $^{3}J_{H-H}$ = 6.9 Hz, $CH(CH_3)_2$), 2.05 (6H, s, CCH_3), 0.98 (12H, d, $^{3}J_{H-H}$ = 6.9 Hz, $CH(CH_3)_2$). $^{13}C\{^{1}H\}$ NMR (75.4 MHz, $CDCl_3$, 298 K): δ 133.4−133.1 (m, $C^{2,6\text{ and }3,5}$H, dppm), 131.2 (d, $^{2}J_{C-P}$ = 2.2 Hz, $C^{2,6\text{ or }3,5}$H, η^6-*p*-cymene), 130.5 (d, $^{2}J_{C-P}$ = 2.1 Hz, $C^{2,6\text{ or }3,5}$H, η^6-*p*-cymene), 129.3 (s, C^{4}H, dppm), 127.4−126.7 (m, C^{1}, dppm (overlapping with signals from **4**)), 126.0 (t, $^{1}J_{C-P}$ = 5.0 Hz, PCH_2P, dppm), 99.1 (s, $C^{1\text{ or }4}$, η^6-*p*-cymene), 86.3 (s, $C^{1\text{ or }4}$, η^6-*p*-cymene), 28.9 (s, $CH(CH_3)_2$), 21.3 (s, $CH(CH_3)_2$), 16.9 (s, CCH_3). $^{31}P\{^{1}H\}$ NMR (121.4 MHz, $CDCl_3$, 298 K): δ −21.8 (s).

2.5. Synthesis of [OsCl(η^6-*p*-cymene)(PPh_3)($GeCl_3$)] (7). One hundred milliliters of dichloromethane was dried by passage through a plug of alumina in a Schlenk flask. Dichloromethane was then degassed prior to other manipulations. A total of 130.0 mg (0.198 mmol) of **3** was added to the Schlenk flask together with 51.0 mg (0.220 mmol, 1.1 equiv) of germanium(II) chloride·dioxane. The mixture was stirred at room temperature under a positive pressure of nitrogen for 1 h. The solvent was then removed *in vacuo* on the Schlenk line. Properties: sparingly soluble in $CDCl_3$ and DMSO and unstable in DMSO. 132.9 mg (0.166 mmol) of yellow solid (84%). Melting point: 245 °C + dec. ^{1}H NMR (300 MHz, $CDCl_3$, 298 K): δ 7.68−7.65 and 7.42−7.40 (15H, both m, PPh_3), 6.19 (1H, d, $^{3}J_{H-H}$ = 5.7 Hz, η^6-C_6H_4), 5.84 (1H, d, $^{3}J_{H-H}$ = 5.6 Hz, η^6-C_6H_4), 5.51 (1H, d, $^{3}J_{H-H}$ = 5.4 Hz, η^6-C_6H_4), 5.02 (1H, dd, $^{3}J_{H-H}$ = 5.6 Hz, $^{4}J_{H-H}$ = 1.4 Hz, η^6-C_6H_4), 3.48 (0.2 **7**·OEt_2), 2.54 (1H, sept, $^{3}J_{H-H}$ = 6.9 Hz, $CH(CH_3)_2$), 1.79 (3H, s, CCH_3), 1.26 (3H, d, $^{3}J_{H-H}$ = 6.9 Hz, $CH(C^{A}H_3CH_3)$), 1.22 (3H, d, $^{3}J_{H-H}$ = 7.0, $CH(CH_3C^{B}H_3)$), 1.21 (0.2 **7**·OEt_2). $^{13}C\{^{1}H\}$ NMR (75.4 MHz, $CDCl_3$, 298 K): δ133.4 (d, $^{Y}J_{C-P}$ = 9.9 Hz, $C^{3,5\text{ or }2,6}$H, PPh_3), 132.6 (d, $^{1}J_{C-P}$ = 55.0 Hz, C^{1}, PPh_3), 129.7 (d, $^{4}J_{C-P}$ = 2.3 Hz, C^{4}H,PPh_3), 127.2 (d, $^{Y}J_{C-P}$ = 10.5 Hz, $C^{2,6\text{ or }3,5}$H, PPh_3), 113.7 (d, $^{2}J_{C-P}$ = 1.7 Hz, $C^{2\text{ or }3\text{ or }5\text{ or }6}$H, η^6-*p*-cymene), 93.2 (s, $C^{1\text{ or }4}$, η^6-*p*-cymene), 84.9 (d, $^{2}J_{C-P}$ = 2.8 Hz, $C^{2\text{ or }3\text{ or }5\text{ or }6}$H, η^6-*p*-cymene), 84.1 (d, $^{2}J_{C-P}$ = 2.2 Hz, $C^{2\text{ or }3\text{ or }5\text{ or }6}$H, η^6-*p*-cymene), 80.2 (s, $C^{1\text{ or }4}$, η^6-*p*-cymene), 79.7 (d, $^{2}J_{C-P}$ = 7.2 Hz, $C^{2\text{ or }3\text{ or }5\text{ or }6}$H, η^6-*p*-cymene), 28.6 (s, $CH(CH_3)_2$), 21.3 (s, $CH(C^{A}H_3CH_3)$), 20.9 (s, $CH(CH_3C^{B}H_3)$), 16.0 (s, CCH_3). $^{31}P\{^{1}H\}$ NMR (121.4 MHz, $CDCl_3$, 298 K): δ −13.73 (s). FTIR (cm^{-1}): 3064 (w), 2962 (w), 2869 (w), 1485 (w), 1433 (m), 1375 (w), 1261 (m), 1161 (w), 1090 (br s), 1017 (br m), 925 (w), 904 (w), 855 (vm), 797 (s), 747 (s), 695 (s). UV/Vis (dichloromethane): λ_{max} = 361 nm. EIMS (70 eV): 802.0 ([OsCl(η^6-*p*-cymene)(PPh_3)$GeCl_3$]$^+$, <1%), 766.0 ([Os(η^6-*p*-cymene)(PPh_3)$GeCl_3$]$^+$, 7.9%), 623.1 ([OsCl(η^6-*p*-cymene)-(PPh_3)]$^+$, 3.5%), 585.1 ([Os(η^6-*p*-cymene)(PPh_3) − H]$^+$, 3.4%), 262.1 ([PPh_3]$^+$, 100%), 152.1 ([$C_{10}H_{14}$ + H_2O]$^+$, 19%). ESI-MS: *m*/*z* calcd. for [M + Na]$^+$, 824.9480; expt., 824.9465.

2.6. Synthesis of [OsCl(η^6-*p*-cymene)-(κ^2dppm)]$^+$$GeCl_3^-$ (8). Procedure 1: A total of 100.2 mg of the nonseparated mixture of **4** and **5** (0.129 mmol, 1 equiv) was dissolved in dichloromethane (100 mL) which was previously dried and degassed, followed by the addition of 34.8 mg (0.150 mmol, 1.2 equiv) of germanium(II) chloride·dioxane. The mixture was stirred under a positive pressure of nitrogen for 1.5 h at room temperature. Upon completion, a bright yellow-green solution was filtered and the solvent was removed *in vacuo*. The resultant brown oil was washed with diethyl ether (3 × 10 mL), and the remaining yellow solid was dried *in vacuo*. A total of 98.0 mg (0.106 mmol) of "lemon chiffon" yellow solid was obtained (yield: 82%). Properties: sparingly soluble in $CDCl_3$ and DMSO, somewhat stable in DMSO, air-stable. Melting point: 246 °C + dec. ^{1}H NMR (300 MHz, $CDCl_3$, 298 K): δ 7.62−7.28 (20H, m, phenyls, dppm), 6.26 (1H, m, $PC^{A}HP$, dppm), 6.20 (2H, d, $^{3}J_{H-H}$ = 5.9 Hz, $C^{2,6\text{ or }3,5}H$, η^6-*p*-cymene), 6.14 (2H, d, $^{3}J_{H-H}$ = 5.8 Hz, $C^{2,6\text{ or }3,5}H$, η^6-*p*-cymene), 4.69 (1H, dt, $^{2}J_X$ = 15.1 Hz, $^{2}J_X$ = 12.7 Hz, $PCH^{B}P$, dppm), 3.48 (0.09 **8**·OEt_2), 2.45 (1H, sept, $^{3}J_{H-H}$ = 6.9 Hz, $CH(CH_3)_2$), 1.67 (3H, s, CCH_3), 1.21 (0.09 **8**·OEt_2), 1.11 (6H, d, $^{3}J_{H-H}$ = 6.9 Hz, $CH(CH_3)_2$). $^{31}P\{^{1}H\}$ NMR (121.4 MHz, $CDCl_3$, 298 K): δ −39.9 (s). FTIR (cm^{-1}): 3060 (w), 2963 (w), 2920 (w), 2869 (w), 1740 (w), 1484 (w), 1435 (m), 1260 (m), 1089 (br s), 1058 (br m), 1018 (br s), 869 (w), 801 (s), 739 (m), 729 (m), 683 (br s), 667 (m). UV/Vis λ_{max} (dichloromethane): 359 nm. ESI-MS: *m*/*z* calcd. for [M]$^+$, 745.1596; expt., 745.1575. Procedure 2: One hundred milliliters of dichloromethane was dried and degassed prior to addition of the reactants. A total of 88.0 mg (0.113 mmol, 1 equiv) of **4** was added to a Schlenk flask together with 39.8 mg (0.172 mmol, 1.5 equiv) of germanium(II) chloride·dioxane. The mixture was stirred at room temperature under a positive pressure of nitrogen for 1 h. The solvent was then evaporated *in vacuo* on the Schlenk line. Air-stable. A total of 83.1 mg (0.090 mmol) of yellow solid was obtained (80%). All the spectra were identical as for compound **8** from Procedure 1.

2.7. Synthesis of [OsCl(η^6-C_6H_6)(PPh_3)($GeCl_3$)] (9). Complex **9** was synthesized following the same procedure as complexes **7**. A total of 142.3 mg (0.237 mmol) of **6** was added to 30 mL of dried and nitrogen-purged dichloromethane. A total of 60.6 mg (0.262 mmol, 1.1 equiv) of germanium(II) chloride·dioxane was then added rapidly to the mixture. The solution was stirred at room temperature under a positive pressure of nitrogen for 1 h. The solvent was then evaporated *in vacuo*, affording the product. Air-stable. A total of 127.7 mg (0.171 mmol) of yellow solid was obtained (72%). Melting point: 265 °C + dec. ^{1}H NMR (300 MHz, $CDCl_3$, 298 K): δ 7.64−7.57 and 7.45−7.42 (15H, both m, PPh_3), 5.71 (6H, s, η^6-C_6H_6), 3.48 (0.5 **9**·OEt_2), 1.21 (0.5 **9**·OEt_2). $^{13}C\{^{1}H\}$ NMR (75.4 MHz, $CDCl_3$, 298 K): δ 134.2 (d, $^{X}J_{C-P}$ = 9.9 Hz, $C^{2,6\text{ or }3,5}$H, PPh_3), 133.0 (d, $^{1}J_{C-P}$ = 56.6 Hz, C^{1}, PPh_3), 131.1 (d, $^{4}J_{C-P}$ = 2.7 Hz, C^{4}H, PPh_3), 128.5 (d, $^{X}J_{C-P}$ = 11.0, $C^{2,6\text{ or }3,5}$H, PPh_3), 85.2 (d, $^{2}J_{C-P}$ = 2.7 Hz, η^6-C_6H_6), 65.9 (**9**·OEt_2), 15.3 (**9**·OEt_2). $^{31}P\{^{1}H\}$ NMR (121.4 MHz, $CDCl_3$, 298 K): δ −12.16 (s). FTIR (cm^{-1}): 3082 (w), 2978 (w), 2867 (w), 1482 (vw), 1433 (m), 1383 (w), 1251 (w), 1184 (w), 1100 (m), 1088 (m), 999 (w), 870 (w), 833 (m), 746 (s), 698 (s), 691 (s), 619 (w). UV/Vis (dichloromethane): λ_{max} = 320 nm. ESI-MS: *m*/*z* calcd. for [M]$^+$, 745.8962; expt., 745.1587; *m*/*z* calcd. for [M + 2ACN + H]$^+$, 828.9565; expt., 829.1587.

2.8. Synthesis of [OsCl(η^6-*p*-cymene)(κ^2-dppm)]$^+$$SnCl_3^-$ (10). One hundred milliliters of dichloromethane was dried over an alumina column and degassed with nitrogen. After dissolving 150.3 mg of the mixture of intermediates **4** and **5** (0.193 mmol, 1 equiv) in dichloro-

https://doi.org/10.1021/acsomega.1c02665
ACS Omega 2021, 6, 19252−19268

methane, 40.3 mg (0.213 mmol, 1.1 equiv) of $SnCl_2$ was added to the bright yellow solution. The mixture was thereafter refluxed under nitrogen for 3.5 h at 60 °C. Upon reaction completion, the murky golden solution was filtered and the filtrate was evaporated to dryness. The resulting brown oil was washed with diethyl ether (3 × 10 mL) and was subsequently dried *in vacuo*. A total of 152.7 mg (0.158 mmol) of a bright, shiny yellow crystalline solid was formed (yield: 82%). Properties: sparingly soluble in $CDCl_3$, readily soluble and stable in DMSO, and air-stable. Melting point: 223 °C + dec. ^{1}H NMR (300 MHz, $CDCl_3$, 298 K): δ 7.64−7.38 (20H, m, dppm), 6.27 (1H, m, PC*H*^{A}HP, dppm), 6.22 (2H, d, $^3J_{H-H}$ = 6.0 Hz, C$^{2,6\text{ or }3,5}$*H*, η^6-*p*-cymene), 6.17 (2H, d, $^3J_{H-H}$ = 6.1 Hz, C$^{2,6\text{ or }3,5}$*H*, η^6-*p*-cymene), 4.69 (1H, dt, ^2J_X = 15.1 Hz, ^2J_X = 12.6 Hz, PCH*H*^{B}P, dppm), 3.48 (0.05 **10**·OEt$_2$), 2.46 (1H, sept, $^3J_{H-H}$ = 6.6 Hz, C*H*(CH$_3$)$_2$), 1.68 (3H, s, CC*H*$_3$), 1.21 (0.05 **10**·OEt$_2$), 1.12 (6H, d, $^3J_{H-H}$ = 6.6 Hz, CH(C*H*$_3$)$_2$). ^{13}C{^{1}H} NMR (75.4 MHz, DMSO, 298 K): δ 132.3−129.0 (m, *C*$^{1-6}$P, dppm), 112.7 (s, *C*$^{1\text{ or }4}$, η^6-*p*-cymene), 96.3 (s, *C*$^{1\text{ or }4}$, η^6-*p*-cymene), 84.8 (t, $^2J_{C-P}$ = 2.5 Hz, *C*$^{2,6\text{ or }3,5}$H, η^6-*p*-cymene), 81.5 (t, $^2J_{C-P}$ = 3.3 Hz, *C*$^{2,6\text{ or }3,5}$H, η^6-*p*-cymene), 43.5 (t, $^1J_{C-P}$ = 33.0 Hz, PCH$_2$P, dppm), 29.9 (s, *C*H(CH$_3$)$_2$), 21.9 (s, CH(*C*H$_3$)$_2$), 16.6 (s, C*C*H$_3$). ^{31}P{^{1}H} NMR (121.4 MHz, $CDCl_3$, 298 K): δ −39.8 (s). FTIR (cm^{-1}): 3062 (w), 2963 (w), 2922 (w), 2867 (w), 1685 (vw), 1559 (vw), 1483 (w), 1435 (m), 1374 (w), 1309 (w), 1260 (w), 1187 (w), 1156 (w), 1101 (m), 1057 (vw), 1025 (vw), 999 (vw), 869 (w), 800 (w), 775 (vw), 743 (vm), 728 (s), 712 (m), 703 (vm), 692 (s), 668 (m), 635 (w). UV/Vis λ_{max} (dichloromethane): 296 nm (major), 269 nm (minor). ESI-MS: *m*/*z* calcd. for [M]$^+$, 745.1596; expt., 745.2011.

2.9. Synthesis of [OsCl(η^6-*p*-cymene)(PPh$_3$)(SnCl$_3$)] (11). In a Schlenk flask, 50 mL of dry dichloromethane was degassed prior to other manipulations. A total of 71.2 mg (0.108 mmol) of **3** was added to the Schlenk flask together with 31.1 mg (0.164 mmol, 1.5 equiv) of tin(II) chloride. The mixture was refluxed under a positive pressure of nitrogen for 17.5 h. The reaction yielded a bright, yellow liquid, which was subsequently filtered. The filtrate was evaporated on a rotary evaporator and washed with diethyl ether. Diethyl ether washings were discarded and the remaining residue was dried *in vacuo* on a Schlenk line. Properties: sparingly soluble in $CDCl_3$ and soluble in DMSO. 73.2 mg (0.086 mmol) of bright orange crystals (80%). Melting point: 239 °C + dec. ^{1}H NMR (300 MHz, $CDCl_3$, 298 K): δ 7.68−7.61 and 7.46−7.41 (15H, m, PPh$_3$), 6.20 (1H, d, $^3J_{H-H}$ = 5.7 Hz, η^6-C$_6$*H*$_4$), 6.15 (1H, d, $^3J_{H-H}$ = 5.7 Hz, η^6-C$_6$*H*$_4$), 5.42 (1H, d, $^3J_{H-H}$ = 5.7 Hz, η^6-C$_6$*H*$_4$), 5.16 (1H, d, $^3J_{H-H}$ = 5.7 Hz, η^6-C$_6$*H*$_4$), 3.48 (0.025 **11**·OEt$_2$), 2.25 (1H, sept, $^3J_{H-H}$ = 7.0 Hz, C*H*(CH$_3$)$_2$), 1.94 (3H, s, CC*H*$_3$), 1.21 (3H, d, $^3J_{H-H}$ = 6.9 Hz, CH(CH$_3$C^A*H*$_3$)), 1.14 (3H, d, $^3J_{H-H}$ = 6.9 Hz, CH(CH$_3$C^B*H*$_3$)). ^{13}C{^{1}H} NMR (75.4 MHz, DMSO, 298 K): δ 134.5 (d, $^1J_{C-P}$ = 56.0 Hz, *C*^{1}, PPh$_3$), 133.9 (d, $^XJ_{C-P}$ = 9.9 Hz, *C*$^{2,6\text{ or }3,5}$H, PPh$_3$), 131.1 (d, $^4J_{C-P}$ = 2.2 Hz, *C*^{4}H, PPh$_3$), 128.7 (d, $^XJ_{C-P}$ = 10.5 Hz, *C*$^{2,6\text{ or }3,5}$H, PPh$_3$), 109.1 (s, *C*$^{1\text{ or }4}$, η^6-*p*-cymene), 97.1 (s, *C*$^{1\text{ or }4}$, η^6-*p*-cymene), 83.1 (d, $^2J_{C-P}$ = 3.3 Hz, *C*$^{2\text{ or }3\text{ or }5\text{ or }6}$H, η^6-*p*-cymene), 82.2 (d, $^2J_{C-P}$ = 2.2 Hz, *C*$^{2\text{ or }3\text{ or }5\text{ or }6}$H, η^6-*p*-cymene), 81.0 (d, $^2J_{C-P}$ = 1.6 Hz, *C*$^{2\text{ or }3\text{ or }5\text{ or }6}$H, η^6-*p*-cymene), 80.5 (d, $^2J_{C-P}$ = 5.0 Hz, *C*$^{2\text{ or }3\text{ or }5\text{ or }6}$H, η^6-*p*-cymene), 29.5 (s, CH(CH$_3$)$_2$), 22.6 (s, CH(C^{A}H$_3$CH$_3$)), 22.5 (s, CH(CH$_3$C^{B}H$_3$), 17.6 (s, CCH$_3$). ^{31}P{^{1}H} NMR (121.4 MHz, $CDCl_3$, 298 K): δ −14.5 (s). FTIR (cm^{-1}): 3803 (w), 3676 (w), 2163 (w), 1734 (w), 1684 (w), 1654 (w), 1559 (w), 1507 (w), 1457 (w), 1436 (m), 1374 (w), 1160 (w), 1091 (m), 1050 (w), 1030 (w), 999 (w), 870 (w), 799 (w), 746 (m), 694 (s). UV/Vis λ_{max} (dichloromethane): 350 nm (major), 311 nm (minor). ESI-MS: *m*/*z* calcd. for [M − SnCl$_3$]$^+$, 623.1310; expt., 623.1658.

2.10. Density Functional Theory Calculations. The ground-state structures of all complexes were determined by density functional theory (DFT) methods, with the resolution of identity approximation[25] using the TURBOMOLE[26] program package and the user interface TmoleX 4.2.[27] The basis set def2-SV(P)[28] was used to pre-optimize the structures. The final optimized structures and orbital occupancies were then calculated using the def2-TZVPP[28] basis set for Sn, Ge, P, Cl, C, and H atoms, with Hay&Wadt ECP-46 for Sn (ECP, effective core potential).[29] The basis set LANL2DZ with Hay&Wadt ECP-60 was used for Os.[29] The hybrid functional B3LYP[30] was used for all calculations. The boundary surface representations of the HOMO and LUMO frontier orbitals are represented with an isosurface of 0.03. Color codes: Sn, purple; Ge, cyan; P, orange; Cl, green; C, olive; H, white; Os, dark blue.

2.11. Cancer Cell Lines. Short-term (24 h) *in vitro* anticancer activities of the synthesized compounds were studied using Dalton's ascites lymphoma (DL) and Ehrlich ascites carcinoma (EAC) malignant cell lines. The cancer cells (DL) were cultured in RPMI-1640 supplemented with 10% FBS, gentamycin (20 mg/mL), streptomycin (100 mg/mL), and penicillin (100 IU) in a CO_2 incubator at 37 °C with 5% CO_2. The exponentially growing cells (80% confluency) were subcultured and used for testing the cytotoxicity and apoptosis potential in the said experiments. All the reagent solutions were autoclaved followed by sterilization by filtration through 0.22 μm membranes.

2.12. MTT-Based Cell Viability Assay. The *in vitro* growth inhibitory effect of synthesized compounds (**3**−**11**) in DL and EAC cancer cell lines was evaluated by the colorimetric MTT assay.[31] The *in vitro* short-term cytotoxicity (24 h) test was carried out at different concentrations (0 and 0.01 to 100 or 400 μM) prepared in PBS (PH: 7.4) in a 96-well cell culture plate (Thermo Scientific, cat. no. 265301). The above dose range was selected considering the permissive cytotoxicity (5−10%) in a normal cell line (PBMCs). The cytotoxicity results of potent complexes were compared with the positive reference drug cisplatin. To evaluate the toxic effect of the aforesaid compounds on normal cells, non-tumorigenic peripheral blood mononuclear cells (PBMCs) were used under the same experimental conditions, compound dosing regimen, and culture times as mentioned above. The detail about the methodology is already described previously.[32] The IC_{50} profiles of all the potent compounds on DL, EAC, and PBMC cell lines were determined from dose−response curves using the nonlinear curve fit. For the IC_{50} plot, the *x* axis was considered as different doses (log concentration) and the *y* axis as the percentage of cell death (cytotoxicity).[33] For IC_{50} calculation in DL and EAC cell lines, higher concentration ranges from 0.01 to 100 μM were tested, whereas in normal cells (PBMCs), the tested concentration ranged from 0.01 to 400 μM. The nonlinear curve fit function used for IC_{50} calculations for the different compounds is as follows:

$$y = A1 + (A2 - A1)/(1 + 10^{((LOGx0-x)\times p)})$$

https://doi.org/10.1021/acsomega.1c02665
ACS Omega 2021, 6, 19252−19268

where A1 refers to the bottom asymptote, A2 refers to the top asymptote, LOGx0 refers to the center, and p refers to the hill slope. The full dose−response curves are available in the Supporting Information.

2.13. Apoptosis Study. Apoptosis, or programmed cell death, is a genetically regulated inherent property of metabolically active cells that eliminates severely damaged cells from the body. The tendency to avoid apoptosis leading to a drug resistance phenotype is a characteristic of most malignant cancers. In the present study, compound-mediated apoptotic cell death was determined by the acridine orange and ethidium bromide (AO/EB) dual staining method.[34] The principle of the assay is based on the fact that acridine orange is taken up by both viable and nonviable cells due to membrane permeability and emits green fluorescence, while ethidium bromide is taken up by apoptotic cells due to membrane damage and emits red fluorescence after intercalation with DNA within the nucleus.[35] Briefly, the cancer cells (1×10^6) were treated with different concentrations (0.01, 0.1, 0.5, 1, 5, and 10 μM) of synthesized compounds for 24 h in a 96-well plate (tissue culture grade, flat-bottom, sterile; Thermo Fisher Scientific, Waltham, Massachusetts, USA). After treatment, cells were washed twice with PBS (PH: 7.4) followed by staining with acridine orange and ethidium bromide (100 μg/mL each in PBS, pH 7.4) for 5 min in a dark cold room. The control and treated cells were examined in three replicates using a fluorescence microscope and photographed (Medlab Solutions Lx400 FLR Fluorescence Microscope). About 1000 cells were counted per group, and the percentage of apoptotic nuclei (orange/red) was calculated based on differential staining patterns.

2.14. Molecular Docking Simulation. The intermolecular interactions between the common template of the synthesized compound and anti-apoptotic target proteins (BCL-2 (PDB: 2O22), BCL-XL (PDB: 1R2D), and MCL-1 (PDB: 6QGD) were studied using Molegro Virtual Docker (Trial MVD 2010.4.0) software for Windows. The docking run was carried out using a GRID of 15 Å in radius and 0.30 in resolution with a number of runs of 10, maximum interactions of 1500, a maximum population size of 50, maximum steps of 300, a neighbor distance factor of 1.00, and a maximum number of poses returned of 5.[36] After molecular docking, the protein−ligand complex was further analyzed and visualized by Chimera software (https://www.cgl.ucsf.edu/chimera/) and BIOVIA Discovery Studio Visualization (https://www.3dsbiovia.com/products/collaborative-science/biovia-discovery-studio/). On the basis of the docking score, the obtained potent compounds were further subjected to pharmacokinetic and druglikeness property calculation using the SwissADME online tool (http://www.swissadme.ch/index.php).[37]

2.15. Statistical Analysis. The experimental results are expressed as mean values ± S.D. All measurements were replicated three times. The data were analyzed by an analysis of variance (ANOVA) ($^*P \leq 0.05$).

3. RESULTS AND DISCUSSIONS

3.1. Synthesis and Spectroscopic Properties of the Neutral Compounds 7, 9, and 11. The precursors $[OsCl_2(\eta^6\text{-}C_6H_6)]_2$ (**1**) and $[OsCl_2(\eta^6\text{-}p\text{-cymene})]_2$ (**2**) were synthesized according to literature procedures *via* redox reactions using $OsCl_3{\cdot}xH_2O$ with 1,3-cyclohexadiene and α-terpinene, respectively.[23a,b] After cleaving the dimers **1** and **2** with PPh_3 (see the Supporting Information), the resulting isolated piano-stool intermediates **3** and **6** were reacted with a slight excess of $GeCl_2{\cdot}$(dioxane), yielding the desired σ-germyl complexes, *via* a facile $GeCl_2$ insertion into the Os−Cl bonds, *rac*-**7** and *rac*-**9**, respectively. Similarly, complex **3** was reacted with an excess of $SnCl_2$ to produce the stannyl complex *rac*-**11** (Scheme 3). Osmium arene complexes bearing a σ-bound

Scheme 3. Synthesis of the Neutral Compounds *rac*-7, *rac*-9, and *rac*-11

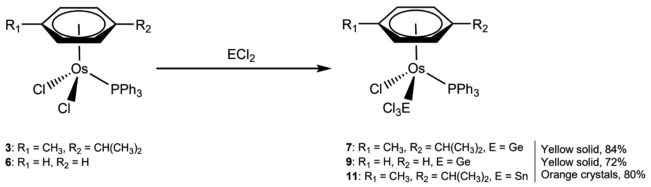

germyl or stannyl group are surprisingly rare in the literature, with only two reports by Wen and co-workers[21] and Castro and co-workers.[22] Detailed biological investigations of these complexes and elucidation of bonding by density functional theory (DFT) methods have not been evaluated and are reported for these complexes.

The ^{1}H and $^{13}C\{^1H\}$ NMR spectra were especially instructive in revealing the structures of the final p-cymene-containing complexes **7** and **11** due to the emerging chirality around the osmium centers upon insertion of Ge or Sn. In fact, complexes **7**, **9**, and **11** exist as a racemic mixture of enantiomers *rac*-**7**, *rac*-**9**, and *rac*-**11**, but we denote only one of the mirror image stereoisomers for simplicity. The aromatic region of the p-cymene ligand in complexes **7** and **9** is represented by four sets of doublet resonances due to asymmetry at the Os center. The ^{i}Pr moiety also has two sets of resonance signals corresponding to $CH(CH_3{}^aCH_3{}^b)$ in the ^{1}H NMR spectrum. This contrasts with the achiral starting material **3**, where the aromatic protons are depicted by two sets of doublets and the one methyl resonance signal for ^{i}Pr, which are equivalent and therefore display a single doublet resonance signal in the ^{1}H NMR spectrum corresponding to $CH(CH_3)_2$. Similar observations are apparent in the $^{13}C\{^1H\}$ NMR spectra of **7** and **11**, and the p-cymene ring carbon atoms are all inequivalent, exhibiting six sets of resonance signals, most of which are doublets due to $^2J_{C-P}$ coupling to the P atom of the phosphine ligand bound to the Os center. The carbons from the methyl groups from ^{i}Pr are also split into two resonance signals, again in contrast with the $^{13}C\{^1H\}$ NMR spectrum of the achiral complex **3**. The $^{31}P\{^1H\}$ NMR spectra of **7**, **9**, and **11** exhibit sharp singlet resonances and only show slight shifts compared to the starting materials **3** and **6**.

3.2. Synthesis and Spectroscopic Properties of the Ionic Compounds 8 and 10. The precursor complex $[OsCl_2(\eta^6\text{-}p\text{-cymene})(\kappa^1\text{-dppm})]$ (**4**) was prepared in two different solvents: dimer **2** was reacted with an excess of dppm (1,1-bis(diphenylphosphino)methane) in (1) acetonitrile (a coordinating solvent) or (2) dichloromethane (a noncoordinating solvent). Strikingly, the nature of the solvent dictates the path that the reaction follows. The reaction in acetonitrile yielded a mixture of the desired **4** and a bidentate κ^2-dppm species (**5**) (Scheme 4), while the reaction in dichloromethane afforded a mixture of complex **4** and a dinuclear complex ($[[OsCl_2(\eta^6\text{-}p\text{-cymene})]_2(\mu\text{-dppm})]$, (**0**) (Scheme 4).

https://doi.org/10.1021/acsomega.1c02665
ACS Omega 2021, 6, 19252−19268

Scheme 4. Solvent-Dependent Pathway to $[OsCl_2(\eta^6\text{-}p\text{-cymene})(\kappa^1\text{-dppm})]$ (4)

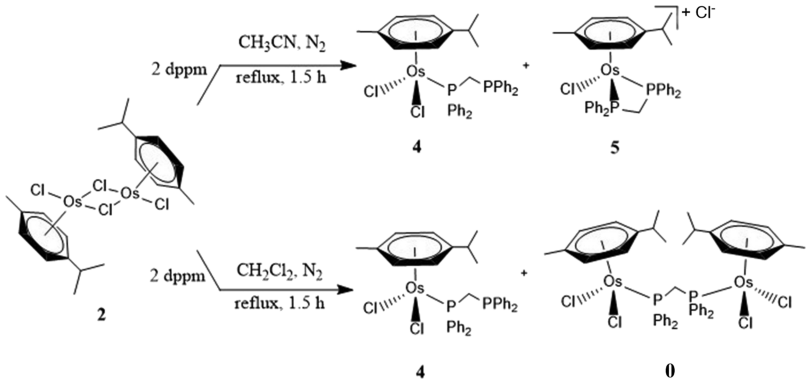

It is likely that the mechanism of the reaction in acetonitrile involves coordination thereof to the osmium center of the formed complex **4**, resulting in **4**−$NCCH_3^+Cl^-$, which then undergoes transformation to **5** with CH_3CN elimination.[38] $^{31}P\{^1H\}$ NMR spectroscopy of the crude reaction mixture in this case showed the clean formation of three resonance signals: two doublets at δ = −16.1 and −28.8 ppm corresponding to complex **4** and a singlet resonance signal for the salt complex **5** at δ = −40.0 ppm. Strikingly, the peaks of the ruthenium analogue of **4**, $[RuCl_2(\eta^6\text{-}p\text{-cymene})(\kappa^1\text{-dppm})]$, can be found at δ = 25.6 and −28.1 ppm.[39] Fortunately, complexes **4** and **5** could be separated by fractional recrystallization using dichloromethane and diethyl ether. In an attempt to surmount the problem of two emerging products, dichloromethane was used instead as a solvent, hoping that the reaction would proceed cleanly to **4** from precursor **2**. However, $^{31}P\{^1H\}$ NMR again indicated two sets of signals with two doublets (δ = −16.1 and −28.8 ppm) and a singlet at δ = −21.8 ppm, corresponding to **4** and a new product, $[[OsCl_2(\eta^6\text{-}p\text{-cymene})]_2(\mu\text{-dppm})]$ (**0**), respectively. The peaks attributed to the suspected compound **0** were in good agreement with the ^1H NMR spectrum of the corresponding known ruthenium dimer $[[RuCl_2(\eta^6\text{-}p\text{-cymene})]_2(\mu\text{-dppm})]$.[39]

With the isolated **4** in hand, the germanate salt **8** could be isolated upon the reaction of complex **4** with Lewis acidic $GeCl_2$·(dioxane) (Scheme 5).

Scheme 5. Synthesis of the Ionic Complex 8 from the Isolated Intermediate 4

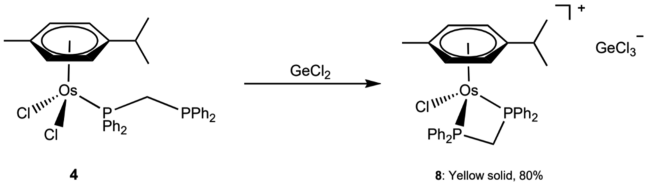

Subsequently, complex **8** could also be selectively synthesized using the mixture of complexes **4** and **5** as a starting material upon reaction with $GeCl_2$·(dioxane), simplifying the synthesis considerably (Scheme 6). Additionally, in close analogy, $SnCl_2$ was reacted with the mixture of **4** and **5**, affording the stannate complex **10** in high yields (Scheme 6).

In the ^1H NMR spectra of salt complexes **8** and **10**, the chelated κ^2 ligand exhibits two sets of resonance signals for the two diastereotopic protons on the dppm bridgehead carbon

Scheme 6. Synthesis of the Ionic Complexes 8 and 10 from a Mixture of 4 and 5

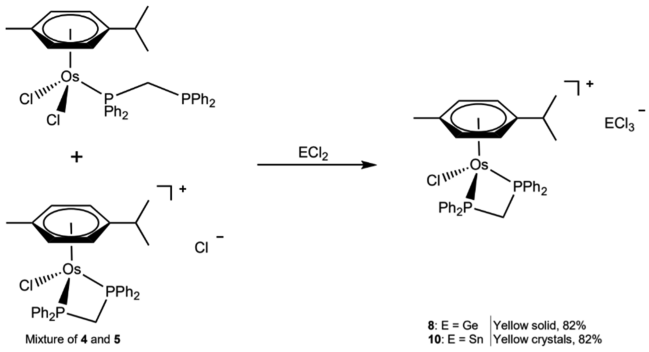

atom due to conformational locking. For both **8** and **10**, these signals appeared as doublets of triplets due to $^2J_{H-H}$ coupling to the other diastereotopic proton and $^2J_{H-P}$ to both P atoms. Interestingly, the chemical shifts of the two protons are several ppm apart in the ^1H NMR spectra, which was confirmed by H,H COSY experiments. The $^{31}P\{^1H\}$ NMR spectra of both salt complexes exhibited sharp singlet resonance signals, which slightly shifted downfield upon the reaction with $GeCl_2$/$SnCl_2$ (δ = −39.9 and −39.8 ppm, respectively). Finally, the cations of both salts were identified with high precision by ESI-MS.

All the final reactions could easily be monitored, as a clear change in color of the solutions could be noticed upon addition of $GeCl_2$ or $SnCl_2$. Final complexes (**7**−**11**) were synthesized successfully with high to excellent yields (72.2−83.8%), and their color ranged from light yellow to dark orange. UV/Vis measurements of compounds **8** and **9** indicated only one maximum peak at 358 and 320 nm, respectively. Intriguingly, two maximum absorptions were observed for compounds **7**, **10**, and **11**.

FTIR spectroscopy was useful in corroborating the presence of a para-substituted *p*-cymene ring and mono-substituted phenyl rings of PPh_3 or dppm ligands. All the vibrations from C−H stretching and bending of alkanes and aromatics were additionally visible. Furthermore, the trichlorogermyl (in **7** and **9**) and trichlorogermanate (in **8**) groups' bonds are hydrolytically robust in contact with air since the wavenumber for hydrolyzed Ge−OH vibration (3571 cm^{-1})[40] was absent from the spectra, nor were any hydrolysis products detected in the NMR spectra.

3.3. DMSO-d_6 Stability Studies. Finally, compounds **7**, **8**, and **10** were tested for stability over time in dimethyl sulfoxide (DMSO-d_6).[41] The testing was performed by recording the

https://doi.org/10.1021/acsomega.1c02665
ACS Omega 2021, 6, 19252−19268

$^{31}P\{^{1}H\}$ and ^{1}H NMR spectra of the complexes dissolved in DMSO-d_6 at various time intervals over a period of 6 h. Complex **10** is stable in DMSO-d_6 for as long as 6 h. This was demonstrated by only one original peak in $^{31}P\{^{1}H\}$ NMR, which does not change over time. Immediately after dissolving compound **8** in DMSO-d_6, some decomposition of the complex occurs, which is demonstrated by a small peak at δ = −23.5 ppm (see the Supporting Information, Figure S29). It appears that it reaches its maximum height after an hour. It is worth mentioning that no visible changes are observed in ^{1}H NMR after 6 h (see the Supporting Information, Figure S30). The germyl complex **7** is somewhat less stable in DMSO-d_6: again, two additional resonance signals arose in the ^{31}P NMR spectrum after only 30 min at δ = −10.2 (doublet) and −26.2 (singlet) ppm, suggesting the formation of other adducts upon dissolution in DMSO-d_6, possibly DMSO adducts (see the Supporting Information, Figure S31). Many studies on the instability of cisplatin and its derivatives (oxaliplatin and carboplatin) in the DMSO solvent have been published.[42] The ruthenium analogue of **7** was also noted to be DMSO-unstable, where the suggested adduct structures consisted of $[(\eta^6\text{-arene})Ru(PR_3)(DMSO)Cl]^+GeCl_3^-$ and $[(\eta^6\text{-arene})Ru(PR_3)(DMSO)GeCl_3]^+Cl^-$[13a] and were linked to the loss of cytotoxic action previously (Scheme 7).

Scheme 7. Potential Structures of the DMSO Adducts of 7[a]

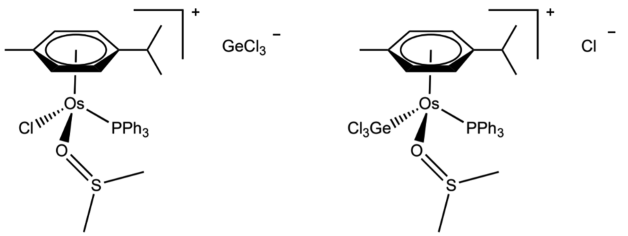

[a]Coordination *via* the S atom of DMSO is also possible.

3.4. Single-Crystal X-ray Diffraction Investigations.

Crystals suitable for X-ray diffraction analysis of **4**, **8**, **9**, **10**, and **11** were grown from dichloromethane or, in some cases, dichloromethane/diethyl ether (see the Supporting Information for complete data).

The precursor compound **4** crystallizes in the monoclinic crystal system with the space group $P2(1)/n$ and adopts a characteristic to such structures, "piano-stool" geometry, with all the angles being less than 90° (Figure 1), except for the CH_2 bridge of dppm (116.8° (2), Table 1). It clearly reveals a pendant phosphorus atom, in accord with our spectral findings.

The germanate complex **8** crystallizes in a monoclinic system as well, with the *Cc* space group. The bonds and angles are observed to be similar as in complex **10**: the longest bond of the cation was between osmium and chlorine, while all the angles are less than 90° (Figure 2), except for the CH_2 dppm bridge and the angles of the anion (Tables 2 and 4). The germanate anion is separated from the cation and is thus a separated ion pair. It exhibits trigonal pyramidal geometry in close similarity to its Ru analogue reported by us earlier.[14]

Complex **9** also crystallizes in the monoclinic crystal system with the space group $P2(1)/n$. The solid-state structure reveals an η^6 coordination of benzene to the osmium center and a distorted tetrahedral geometry around the Os center (Figure 3). The Os−Ge bond length of 2.450 Å lies close to the sum of the single-bond covalent radii of Os and Ge (2.40 Å) and can thus be considered a single bond. Selected bond lengths and bond angles are reported in Table 3.

Complex **10** was found to be in a monoclinic crystal system with the *Cc* space group. Similar to the precursor **4**, all the osmium-related angles are less than 90° (Figure 4). As with the

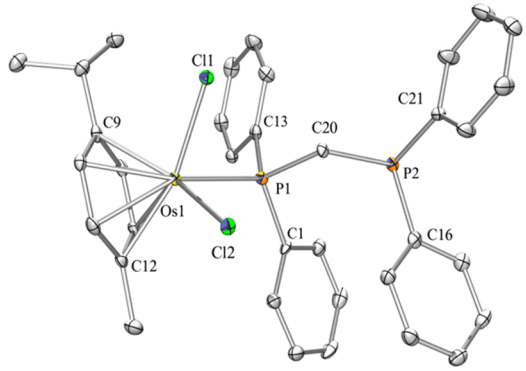

Figure 1. ORTEP representations of complex **4** at the 30% probability level. H atoms are omitted for clarity.

Table 1. Selected Bond Lengths and Angles of the Intermediate 4

selected bond lengths [Å]	
Os(1)−P(1)	2.3562(12)
Os(1)−Cl(1)	2.4208(11)
Os(1)−Cl(2)	2.4265(10)
P(1)−C(20)	1.841(4)
P(2)−C(20)	1.854(4)
selected bond angles [°]	
P(1)−C(20)−P(2)	116.8(2)
P(1)−Os(1)−Cl(1)	83.76(4)
P(1)−Os(1)−Cl(2)	86.46(4)
Cl(1)−Os(1)−Cl(2)	87.88(4)

Table 2. Selected Bond Lengths and Angles of Complex 8

selected bond lengths [Å]	
Os(1)−P(1)	2.3193(19)
Os(1)−P(2)	2.3336(16)
Os(1)−Cl(7)	2.3990(14)
Ge(1)−Cl(1)	2.294(5)
selected bond angles [°]	
P(1)−Os(1)−Cl(7)	82.73(6)
P(2)−Os(1)−Cl(7)	81.53(5)
P(1)−Os(1)−P(2)	70.56(5)
P(1)−C(23)−P(2)	94.1(3)
Cl(2)−Ge(1)−Cl(1)	95.0(7)

Table 3. Selected Bond Lengths and Angles of Complex 9

selected bond lengths [Å]	
Os(1)−P(1)	2.354(3)
Os(1)−Cl(4)	2.412(3)
Os(1)−Ge(2)	2.450(12)
selected bond angles [°]	
P(1)−Os(1)−Cl(4)	88.84(10)
P(1)−Os(1)−Ge(2)	93.36(7)
Cl(4)−Os(1)−Ge(2)	87.91(7)
Cl(1)−Ge(2)−Os(1)	122.80(8)

https://doi.org/10.1021/acsomega.1c02665
ACS Omega 2021, 6, 19252−19268

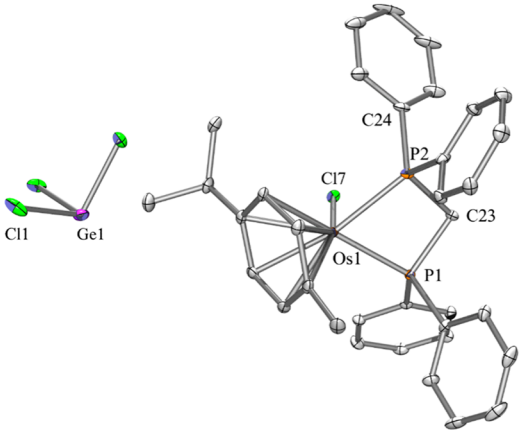

Figure 2. ORTEP representations of complex **8** at the 30% probability level. H atoms are omitted for clarity. The minor component of the disordered $GeCl_3^-$ is also removed for clarity.

Table 4. Selected Bond Lengths and Angles of Complex 10

selected bond lengths [Å]	
Os(1)−P(1)	2.3347(12)
Os(1)−P(2)	2.3162(13)
Os(1)−Cl(1)	2.4001(11)
Sn(1)−Cl(2)	2.4379(18)
selected bond angles [°]	
P(1)−Os(1)−Cl(1)	81.41(4)
P(2)−Os(1)−Cl(1)	82.85(5)
P(2)−Os(1)−P(1)	70.54(4)
P(2)−C(34)−P(1)	94.0(2)

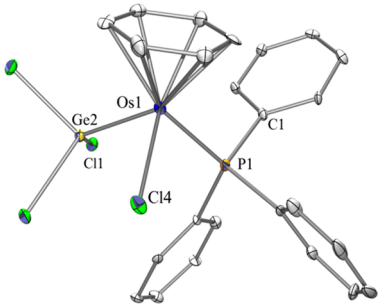

Figure 3. ORTEP representations of complex *rac*-**9** at the 30% probability level. H atoms are omitted for clarity.

germanium analogue, a large distance separates the trigonal pyramidal tin center in the anion from the osmium center and is thus a separated ion-pair salt.

The orthorhombic crystal system with the space group *Pca*2(1) was adopted by the neutral stannyl compound **11**. Similar to **9**, the complex has a distorted tetrahedral geometry (Figure 5) with the Os−Sn bond length of 2.5934(9) Å being slightly shorter than the sum of covalent single-bond radii of osmium and tin (2.69 Å) but can be considered a single bond based on these data (Table 5).

3.5. Quantum Chemical DFT Calculations. Density functional theory calculations (B3LYP, basis set LANL2DZ for Os, and def2-TZVPP for Sn, Ge, Cl, P, C, and H) were employed to gain insights into the electronic nature of the complexes synthesized. The obtained geometry-optimized structure of complex **9** is in good agreement with the experimentally determined X-ray crystal structure (Table 6),

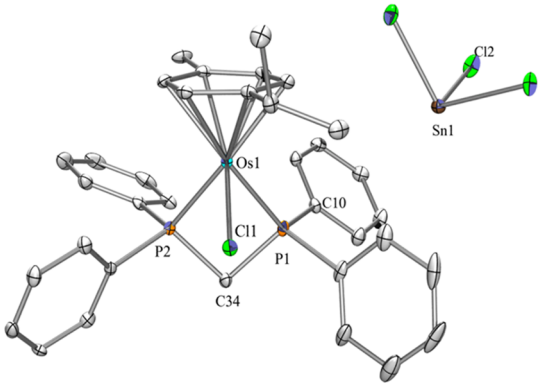

Figure 4. ORTEP representations of complex **10** at the 30% probability level. H atoms are omitted for clarity. The minor component of the disordered $SnCl_3^-$ is also removed for clarity.

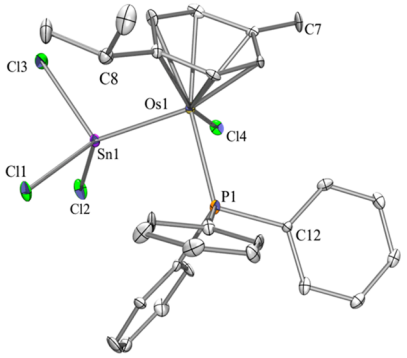

Figure 5. ORTEP representations of complex **11** at the 30% probability level. H atoms are omitted for clarity.

Table 5. Selected Bond Lengths and Angles of Complex 11

selected bond lengths [Å]	
Os(1)−P(1)	2.344(4)
Os(1)−Cl(4)	2.412(3)
Os(1)−Sn(1)	2.5934(9)
selected bond angles [°]	
P(1)−Os(1)−Cl(4)	87.58(11)
P(1)−Os(1)−Sn(1)	91.38(9)
Cl(4)−Os(1)−Sn(1)	84.29(8)
Cl(1)−Sn(1)−Os(1)	121.96(10)
Cl(2)−Sn(1)−Os(1)	127.07(10)
Cl(3)−Sn(1)−Os(1)	111.70(10)

Table 6. Selected Bond Lengths and Bond Angles, Both from the X-ray Crystal Structure and Geometry Optimization, of Complex 9

	selected bond lengths (Å)	
bonds	X-ray crystal structure	DFT calculation
Os(1)−P(1)	2.354(3)	2.393
Os(1)−Cl(4)	2.412(3)	2.439
Os(1)−Ge(2)	2.450(12)	2.504
	selected bond angles (°)	
angles	X-ray crystal structure	DFT calculation
P(1)−Os(1)−Cl(4)	88.84(10)	85.06
P(1)−Os(1)−Ge(2)	93.36(7)	94.85
Cl(4)−Os(1)−Ge(2)	87.91(7)	86.47

https://doi.org/10.1021/acsomega.1c02665
ACS Omega 2021, 6, 19252−19268

with the exception of the phenyl rings of PPh_3, which have a slightly different orientation in the optimized structure compared to the crystal structure (see the Supporting Information, Section 11, for complete DFT data).

Geometry optimization of the benzene analogue of complex **11**, **11−benzene**, was also performed to evaluate the structural changes that could arise from the substitution of Ge for Sn. It appeared that both geometries are fairly similar, the only noticeable difference being the bond lengths of Os−E, which is longer in **11−benzene**, as expected, due to the longer covalent radius of Sn vs Ge (Table 7).

Table 7. Selected Bond Lengths and Bond Angles from the Geometry Optimizations of Complexes 9 and the Theoretical Complex 11−Benzene

	selected bond lengths (Å)	
bonds	**9** (E = Ge)	**11−benzene** (E = Sn)
Os−P	2.393	2.378
Os−Cl	2.439	2.445
Os−E	2.504	2.654
	selected bond angles (°)	
angles	**9** (E = Ge)	**11−benzene** (E = Sn)
P−Os−Cl	85.06	85.57
P−Os−E	94.85	94.19
Cl−Os−E	86.47	85.76

The frontier molecular orbitals of **9** and **11−benzene** were also calculated to evaluate what changes in orbital energies and compositions could arise from the substitution of Ge by Sn in such complexes (Figure 6). The frontier molecular orbitals are virtually the same in composition in **9** and **11−benzene**, with a LUMO majorly localized on the ECl_3 group and spreading through the Os center and the arene ring, with smaller contribution of the Cl bound to Os. The HOMO however shows greater contribution from the Cl bound to the Os center and is also delocalized around E and the arene ring. The PPh_3 moiety does not seem to play any role in the composition of the HOMO and LUMO frontier orbitals in both **9** and **11−benzene**.

The Wiberg bond indices were also calculated for both complexes **9** and **11−benzene**, revealing values close to unity for the Os−E bond (for E = Ge, WBI = 0.792, and for E = Sn, WBI = 0.921). This corroborates the findings of the X-ray analyses, in which, on comparison to covalent radii, the bonds could be considered as single bonds for both the germyl and stannyl complexes.

3.6. *In Vitro* Cell Viability. The evaluation of cell proliferation is often used in medicinal chemistry research as well as the cytotoxicity screening of other biologically active compounds. The MTT assay is based on the ability of the treated cells to convert the water-soluble MTT (3-(4,5-dimethylthiazol-2-yl)-2,5-diphenyltetrazolium bromide) into an insoluble formazan crystal by NADPH-dependent cellular oxidoreductase enzymes. The end product, formazan crystal, is then solubilized and the concentration is determined by the optical density at 570 nm.[43] This method is also used as an important parameter to estimate the cellular energy capacity of the cells.[44] The cytotoxic potential of the synthesized compounds was studied against DL and EAC cell lines at different concentrations. A concentration-dependent decrease in cell viability (increase in cytotoxicity) was observed in both cell lines (Figures 7 and 8). Compound **9** has significantly induced more cytotoxicity in DL cells followed by compounds **8**, **10**, **11**, **7**, and **3**. Interestingly, an almost similar pattern of cytotoxicity was also observed in the case of the EAC cell line. On the other hand, a negligible cytotoxic effect was observed in

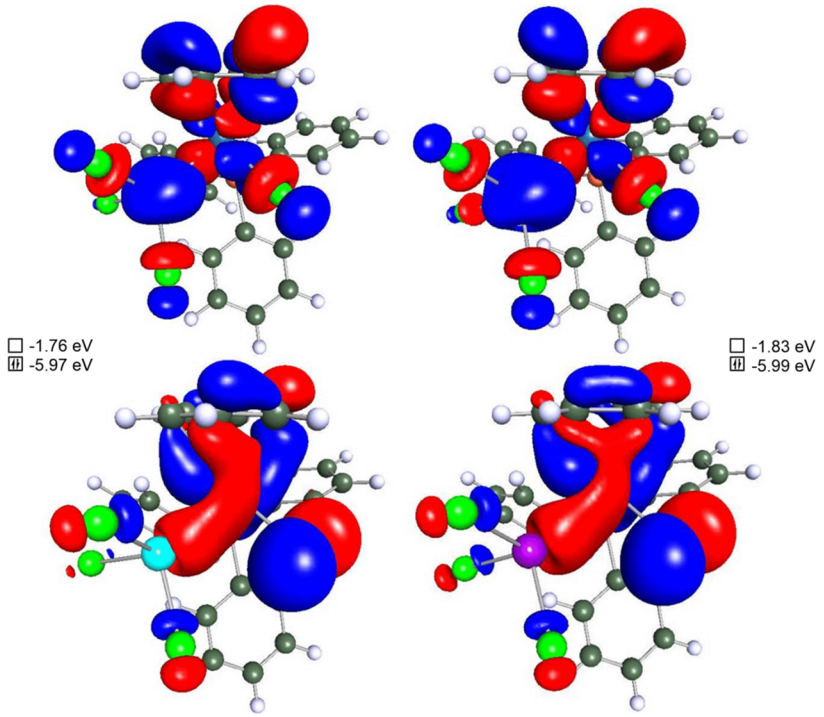

Figure 6. Boundary surface representations of HOMO (bottom) and LUMO (top) for complexes **9** (left) and **11−benzene** (right) and relative energies (HOMO (bottom) and LUMO (top) in eV).

https://doi.org/10.1021/acsomega.1c02665
ACS Omega 2021, 6, 19252−19268

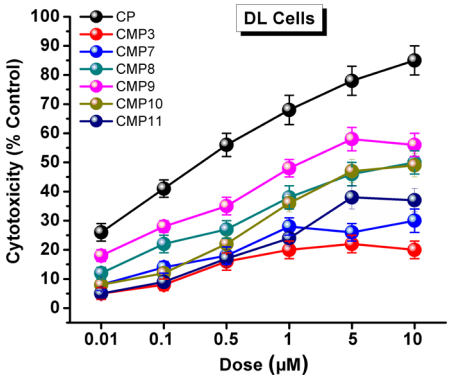

Figure 7. Compound-mediated percent cell cytotoxicity in DL cells after treatment with different dosages. Cisplatin was used as a positive (reference drug) control. Data are mean ± S.D., n = 3. CP, cisplatin; CMP, compound. Only the concentrations up to 10 μM are shown; see the Supporting Information for the other data.

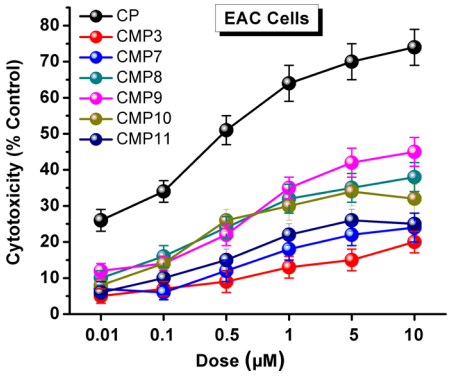

Figure 8. Compound-mediated percent cell cytotoxicity in EAC cells after treatment with different dosages. Cisplatin was used as a positive (reference drug) control. Data are mean ± S.D., n = 3. CP, cisplatin; CMP, compound. Only the concentrations up to 10 μM are shown; see the Supporting Information for the other data.

normal cells (PBMCs) as compared to DL and EAC cell lines (Figure 9), suggesting that the complexes exhibit some selectivity toward the cancer cells. The IC_{50} (half-maximal inhibitory concentration) is a crucial pharmacodynamic index of drug efficacy. The dose−response relationship must be

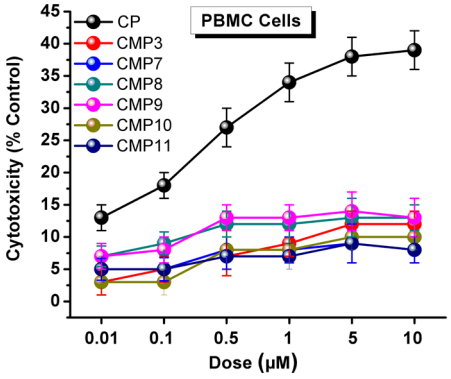

Figure 9. Compound-mediated percent cell cytotoxicity in normal cells (PBMCs) after treatment with different concentrations. Cisplatin was used as a positive (reference drug) control. Data are mean ± S.D., n = 3. CP, cisplatin; CMP, compound. Only the concentrations up to 10 μM are shown; see the Supporting Information for the other data.

defined before this value can be measured, which is normally done by fitting monotonic sigmoidal models. The IC_{50} of drug candidates can be determined by constructing a dose−response curve and examining the effect of different concentrations on biological response that reduced to 50%. The obtained IC_{50} values for the potent compounds on the PBMC cell lines are presented in Table 8, and all dose−response curves are available in the Supporting Information.

It is striking to note that although all complexes exhibit less cytotoxicity compared to the positive control, the best performing complexes in this series are the germanium-containing neutral complex **9** and the germanate salt (**8**). A previous study from our group revealed that ruthenium germyl complexes exhibit almost no cytotoxicity against the cancer cell line A2780 and the healthy cell line HEK-293.[13a] This was attributed to rapid exchange kinetics, where coordination of water to the Ru center occurred rapidly, for which there was spectroscopic evidence. In the present case, the neutral germyl complex **9** exhibits much more potent cytotoxicity, which is likely due to the more inert osmium center. Also, it is worth pointing out that complex **9**, the best performing complex in this series, exhibits a higher selectivity index (SI) compared to cisplatin (82.9 on the DL cell line vs 79.2 for cisplatin), where SI = IC_{50} (PBMC)/IC_{50} (DL).

3.7. Apoptosis Investigations. Apoptosis is a form of genetically programmed cell death mechanism that regulates multicellular organisms' growth by maintaining a balance between cell proliferation and cell death by eliminating physiologically redundant, physically damaged, and abnormal cells.[45] Resistance to apoptosis is a characteristic feature of all types of cancer; therefore, current research focusing on the genes and signals regulating apoptosis has played an important role in cancer research. Most chemotherapeutic drugs destroy tumor cells and restrain their normal cell proliferation rate primarily by inducing apoptosis.[46] In the present study, the acridine orange/ethidium bromide (AO/EB) dual staining method was used to evaluate compound-mediated apoptotic and viable cells in treated groups. Apoptosis-associated changes in treated cells caused an increase in membrane permeability of ethidium bromide and hence made cells appear red, whereas viable cells appeared green.[47] Treatment of DL and EAC cell lines with different compounds (**3** and **7**−**11**) led to the development of apoptotic features that included membrane blebbing, nuclear condensation, and apoptotic bodies (Figure 10). Furthermore, findings from several other studies indicated that the majority of the synthesized compounds had anticancer properties as a result of the formation of stable DNA adducts.[48] It is worth noting that cancer cells have a higher oxidative status than normal cells, which means that they may undergo more oxidative DNA damage than the normal cells. The compounds **8** and **9** have shown a stronger apoptosis-inducing ability than the rest of the tested compounds in the DL cell line (Figure 11). Almost similar results were also obtained in the EAC cell line (Figure 12). Thus, based on the present cytotoxicity and apoptosis assays, it is evident that compounds **8** and **9** possess promising anticancer activity that needs further study to establish the molecular mode of action.

3.8. Molecular Docking Simulations. Molecular docking has become an important bioinformatics tool in the medicinal chemistry field to elucidate fundamental biochemical processes by analyzing the interacting behavior of molecules in the active site of a receptor.[49] The results of molecular docking further corroborate the findings obtained by MTT and apoptosis

https://doi.org/10.1021/acsomega.1c02665
ACS Omega 2021, 6, 19252−19268

Table 8. IC_{50} Values of All Compounds on DL, EAC, and PBMC Cell Lines[a]

	IC_{50} (μM)						
cells	cisplatin	3	7	8	9	10	11
DL cells	0.19 ± 0.07	112 ± 3.4	93 ± 2.8	8.3 ± 0.05	1.7 ± 0.06	15.8 ± 0.05	63.7 ± 1.3
SI PBMC/DL	79.15	1.33	4.28	19.42	82.88	9.18	6.72
EAC cells	0.37 ± 0.10	122.8 ± 2.8	103.8 ± 0.82	18.2 ± 0.05	13.7 ± 0.03	21.4 ± 0.57	87.3 ± 1.6
SI PBMC/EAC	40.64	1.22	3.83	8.86	10.28	6.78	4.90
PBMCs	15.04 ± 0.05	149.9 ± 1.2	397.6 ± 3.5	161.2 ± 2.8	140.9 ± 1.5	145.1 ± 1.8	428.1 ± 3.1

[a]Dose−response curves were used for the calculation of IC_{50}. SI refers to the selectivity index computed by IC_{50} (PBMC)/IC_{50} (DL or EAC).

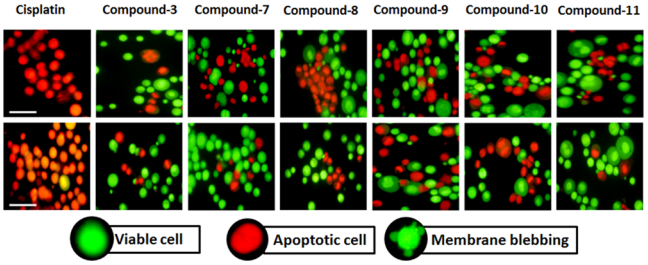

Figure 10. Morphological features of viable and apoptotic cells observed under a fluorescence microscope. Treated cells showing an apoptotic nucleus with membrane damage and chromatin condensation. Cisplatin was used as a reference drug.

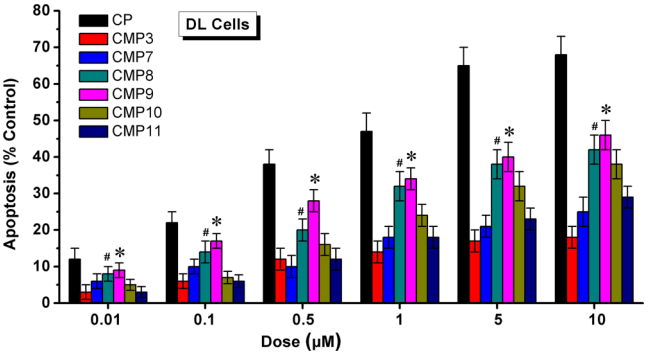

Figure 11. Percentage of apoptotic cells after treatment with different compounds in the DL cell line. Data are mean ± S.D., $n = 3$, one-way ANOVA; $^{*}P \leq 0.05$ as compared to compounds **3**, **7**, **8**, **10**, and **11**, whereas $^{\#}P \leq 0.05$ as compared to compounds **3**, **7**, **10**, and **11**.

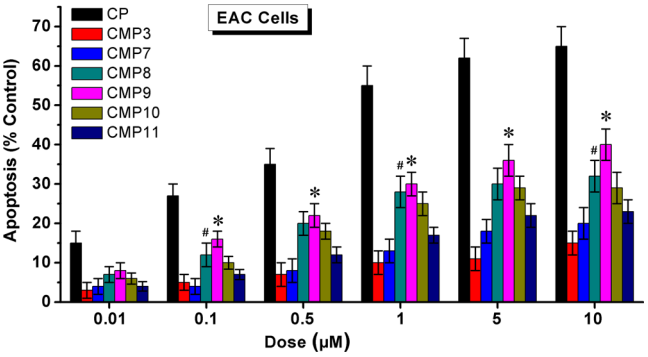

Figure 12. Percentage apoptotic cells after treatment with different compounds in the EAC cell line. Data are mean ± S.D., $n = 3$, one-way ANOVA; $^{*}P \leq 0.05$ as compared to compounds **3**, **7**, **8**, **10**, and **11**, whereas $^{\#}P \leq 0.05$ as compared to compounds **3**, **7**, **10**, and **11**.

assays. Anti-apoptotic proteins, mostly BCL-2, BCL-XL, MCL-1, and many others, are well known to interact with pro-apoptotic proteins to execute apoptosis events.[50] Therefore, molecular docking was performed with the above-mentioned anti-apoptotic target proteins to further dissect the possible molecular mode of action of synthesized compounds. The high expression of BCL-2, BCL-XL, and MCL-1 proteins is reported in multiple cancer types that ultimately induced malignant phenotypes by skipping apoptosis. Moreover, their inhibition by various chemotherapeutic agents is associated with the apoptotic induction, and hence, regression in tumor cell proliferation occurs. Our finding (Figures 13 and 14) showed that complex **9** has high affinity with BCL-2 family proteins. The $\pi-\pi$ stacked and π−alkyl interactions have been found to be greatly involved with the active site amino acids of all the receptors (BCL-2, BCL-XL, and MCL-1). Compound **9** showed one $\pi-\pi$ stacked (Tyr199) and two π−alkyl (Ala97 and Val145) interactions with BLC-2, two $\pi-\pi$ stacked (Tyr195) and two π−alkyl (Ala93 and Val141) interactions with BCL-XL, and one $\pi-\pi$ stacked (Phe270) and four π−alkyl (Val253, Met231, Arg263, and Leu267) interactions with MCL-1. Thus, based on the docking results, it can be suggested that compound **9** possesses an apoptotic-inducing ability due to efficient interaction with anti-apoptotic target proteins. Interestingly, the docking score of complex **9** is found to be comparable with the reference ligands (PDB ID) of the respective receptors (Figure 14). Although these *in silico* studies provide useful insights into the potential mechanism at play for the germyl complex **9** and mirror the findings of the MTT assay and apoptosis studies, additional experimental binding studies are required to confirm this. In addition, in our study, we used the neutral form of complex **9**, whereas dissociation into ionic species is very likely under biological conditions (see Section 3.3).

To be successful as a drug candidate, a potent molecule must reach its target in an adequate concentration and remain there in a bioactive form long enough for the expected biologic events to occur. The drug development process involves assessment of absorption, distribution, metabolism, and excretion (ADME) at a stage when considered compounds are numerous, but access to the physical samples is limited.[37] In that context, we performed the pharmacokinetic and druglikeness study of the compounds. Pharmacokinetics is the study of chemical metabolism and the discovery of a chemical's fate from the time it is delivered until it is totally removed from the body. All the tested compounds showed high GI absorption and no blood−brain barrier (BBB) permeant (Table 9). Druglikeness is a qualitative concept used in drug design that describes how drug-like substances behave in terms of bioavailability. It is estimated from the molecular descriptors before the substance is even synthesized and tested for bioactivities. Druglikeness molecular properties of synthesized compounds were tested and found to pass Lipinski, Ghose, Veber, Egan, and Muegge experiments (Table 9), considering the permissive limit. Pharmacokinetic and

https://doi.org/10.1021/acsomega.1c02665
ACS Omega 2021, 6, 19252−19268

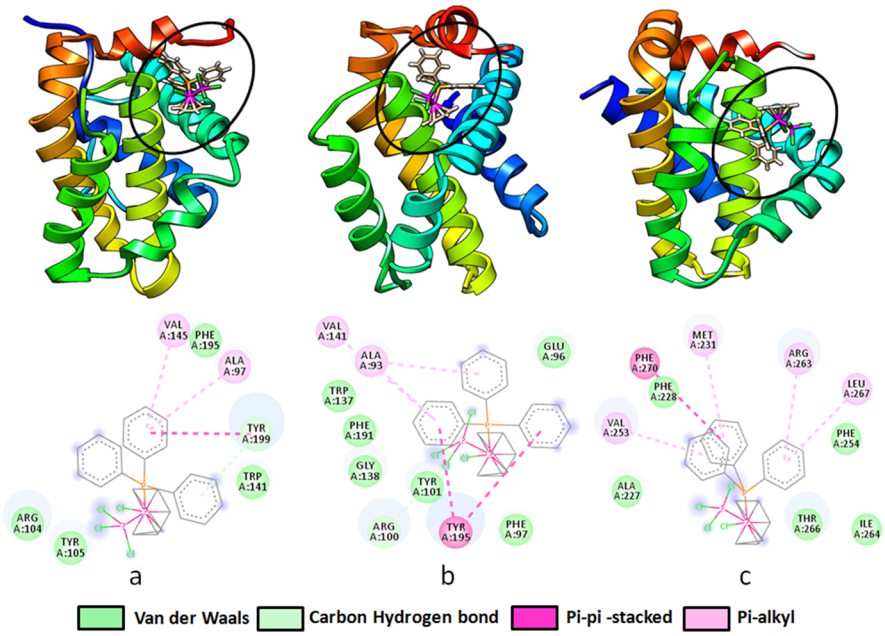

Figure 13. Docking structures of **9** with (a) BCL-2, (b) BCL-XL, and (c) MCL-1 receptors are shown. Chemical interactions are shown along with ligand atoms and interacting amino acids in the inhibitor binding sites of different receptors.

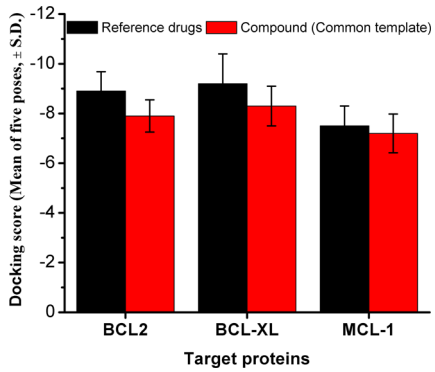

Figure 14. Binding affinities of **9** with BCL-2, BCL-XL, and MCL-1 receptors. Data are mean ± S.D., n = 5.

Table 9. Pharmacokinetic and Druglikeness Properties of Synthesized Compounds (3 and 7−11)

pharmacokinetic properties	compounds					
	3	**7**	**8**	**9**	**10**	**11**
GI absorption	high	high	high	high	high	high
BBB permeant	no	no	no	no	no	no
P-gp substrate	yes	yes	yes	yes	yes	yes
CYP1A2 inhibitor	no	no	no	no	no	no
CYP2C19 inhibitor	no	no	no	no	no	no
CYP2D6 inhibitor	yes	no	no	no	no	yes
CYP3A4 inhibitor	no	yes	no	no	yes	yes
water solubility	no	yes	yes	yes	yes	no

	compounds					
druglikeness	**3**	**7**	**8**	**9**	**10**	**11**
Lipinski	no	yes	yes	yes	yes	no
Ghose	yes	yes	yes	yes	yes	yes
Veber	yes	yes	yes	yes	yes	yes
Egan	yes	no	yes	yes	yes	no
Muegge	yes	no	yes	yes	yes	yes

druglikeness properties of compounds **3** and **7−11** revealed that compounds **8−10** possess strong pharmacokinetic and druglikeness properties (Table 9) that need to be further explored for better understanding of their molecular mode of action. This is also in accord with the *in vitro* apoptosis and docking study.

4. CONCLUSIONS

The synthesis of osmium-based germyl or stannyl/germanate and stannate complexes characterized by FTIR, ^{1}H, ^{13}C{^{1}H}, and ^{31}P{^{1}H} NMR, MP, UV/Vis, ESI-MS, and X-ray diffraction analysis was reported and subjected to anticancer studies. Complexes **3** and **7−11** showed moderate cytotoxic activity on two cell lines *in vitro* compared to cisplatin. Strikingly, the germyl complex **9** exhibited the most promising cytotoxic activity in this series of compounds in contrast to the ruthenium analogues, which were completely inactive, which was potentially due to enhanced stability toward aquation compared to the more labile Ru analogues. Compounds **8** and **9** significantly ($P \leq 0.05$) induced cell cytotoxicity in DL and EAC cell lines by inducing apoptotic cell death with negligible cytotoxicity in healthy PBMCs. The molecular mode of action might involve anti-apoptotic proteins as confirmed by our docking studies, but additional biological investigations and experimental studies need to be conducted to confirm this, along with other studies on other biochemical targets.

■ ASSOCIATED CONTENT

Supporting Information

The Supporting Information is available free of charge at https://pubs.acs.org/doi/10.1021/acsomega.1c02665.

Spectral (NMR, IR, UV/Vis, and ESI-MS) data, X-ray structural parameters, and DFT-optimized structures along with Cartesian coordinates (PDF)

Crystallographic data of compounds **4** and **8−11** (CIF)

https://doi.org/10.1021/acsomega.1c02665
ACS Omega 2021, 6, 19252−19268

AUTHOR INFORMATION

Corresponding Authors

Akalesh Kumar Verma − *Department of Zoology, Cell & Biochemical Technology Laboratory, Cotton University, Guwahati 781001, India*; Email: akhilesh@cottonuniversity.ac.in

Burgert Blom − *Maastricht Science Programme, Faculty of Science and Engineering, Maastricht University, 6200 MD Maastricht, The Netherlands*; orcid.org/0000-0003-3194-0516; Email: burgert.blom@maastrichtuniversity.nl

Authors

Tomiris Nabiyeva − *Maastricht Science Programme, Faculty of Science and Engineering, Maastricht University, 6200 MD Maastricht, The Netherlands*

Basile Roufosse − *Maastricht Science Programme, Faculty of Science and Engineering, Maastricht University, 6200 MD Maastricht, The Netherlands*

Matylda Odachowski − *Maastricht Science Programme, Faculty of Science and Engineering, Maastricht University, 6200 MD Maastricht, The Netherlands*

Judith Baumgartner − *Institut für Anorganische Chemie, Technische Universität Graz, A-8010 Graz, Austria*; orcid.org/0000-0002-9938-1813

Christoph Marschner − *Institut für Anorganische Chemie, Technische Universität Graz, A-8010 Graz, Austria*; orcid.org/0000-0001-8586-2889

Complete contact information is available at: https://pubs.acs.org/10.1021/acsomega.1c02665

Author Contributions

[‖]T.N. and B.R. contributed equally to this work as concurrent first authors. M.O. was involved in the synthesis of some complexes and analysis and contributed to some writing. C.M. and J.B. carried out all X-ray analyses and A.K.V. performed the biological studies. The synthesis was carried out under the supervision of B.B. in his laboratory.

Notes

The authors declare no competing financial interest.

The X-ray structures are deposited in the CCDC at CCDC-2073122 (**4**), 2073121 (**8**), 2073120 (**9**), 2073123 (**10**), and 2073124 (**11**).

ACKNOWLEDGMENTS

Maastricht University and the Faculty of Science and Engineering (FSE) are acknowledged for financial support of this work as well as a grant from SWOL (Stichting Universiteitsfonds Limburg). Numerous students are also thanked for participating in some aspects of research. Dr. M. Schlangen-Ahl (TU Berlin) is thanked for recording some ESI-MS spectra, and Prof. Dr. M. Honing and several members of his group (FHML, Maastricht University) are also thanked for recording some ESI-MS spectra.

REFERENCES

(1) (a) Siegel, R. L.; Miller, K. D.; Jemal, A. Cancer statistics, 2019. *Ca-Cancer J. Clin.* **2019**, *69*, 7−34. (b) Rausch, M.; Dyson, P. J.; Nowak-Sliwinska, P. Recent Considerations in the Application of RAPTA-C for Cancer Treatment and Perspectives for Its Combination with Immunotherapies. *Adv. Ther.* **2019**, *2*, 1900042.

(2) (a) Baskar, R.; Lee, K. A.; Yeo, R.; Yeoh, K.-W. Cancer and radiation therapy: current advances and future directions. *Int. J. Med. Sci.* **2012**, *9*, 193−199. (b) Konkankit, C. C.; Marker, S. C.; Knopf, K. M.; Wilson, J. J. Anticancer activity of complexes of the third row transition metals, rhenium, osmium, and iridium. *Dalton Trans.* **2018**, *47*, 9934−9974.

(3) Simpson, P. V.; Desai, N. M.; Casari, I.; Massi, M.; Falasca, M. Metal-based antitumor compounds: beyond cisplatin. *Future Med. Chem.* **2019**, *11*, 119−135.

(4) Aggarwal, S. Targeted cancer therapies. *Nat. Rev. Drug Discov.* **2010**, *9*, 427−428.

(5) (a) Rosenberg, B.; Van Camp, L.; Krigas, T. Inhibition of Cell Division in Escherichia coli by Electrolysis Products from a Platinum Electrode. *Nature* **1965**, *205*, 698−699. (b) O'Dwyer, P. J.; Stevenson, J. P.; Johnson, S. W. Clinical pharmacokinetics and administration of established platinum drugs. *Drugs* **2000**, *59*, 19−27. (c) Ndagi, U.; Mhlongo, N.; Soliman, M. Metal complexes in cancer therapy - an update from drug design perspective. *Drug Des., Dev. Ther.* **2017**, *11*, 599−616. (d) Go, R. S.; Adjei, A. A. Review of the comparative pharmacology and clinical activity of cisplatin and carboplatin. *J. Clin. Oncol.* **1999**, *17*, 409−409. (e) Abedini, M. R.; Qiu, Q.; Yan, X.; Tsang, B. K. Possible role of FLICE-like inhibitory protein (FLIP) in chemoresistant ovarian cancer cells in vitro. *Oncogene* **2004**, *23*, 6997−7004.

(6) (a) Oun, R.; Moussa, Y. E.; Wheate, N. J. The side effects of platinum-based chemotherapy drugs: a review for chemists. *DaltonTrans.* **2018**, *47*, 6645−6653. (b) Miller, R. P.; Tadagavadi, R. K.; Ramesh, G.; Reeves, W. B. Mechanisms of Cisplatin nephrotoxicity. *Toxins* **2010**, *2*, 2490−2518. (c) Tsang, R. Y.; Al-Fayea, T.; Au, H.-J. Cisplatin Overdose. *Drug Saf.* **2009**, *32*, 1109−1122. (d) Wong, E.; Giandomenico, C. M. Current status of platinum-based antitumor drugs. *Chem. Rev.* **1999**, *99*, 2451−2466.

(7) (a) Brabec, V.; Kasparkova, J. Modifications of DNA by platinum complexes: relation to resistance of tumors to platinum antitumor drugs. *Drug Resist. Updates* **2005**, *8*, 131−146. (b) Rocha, C. R. R.; Silva, M. M.; Quinet, A.; Cabral-Neto, J. B.; Menck, C. F. M. DNA repair pathways and cisplatin resistance: an intimate relationship. *Clinics* **2018**, *73*, e478s. (c) Rabik, C. A.; Dolan, M. E. Molecular mechanisms of resistance and toxicity associated with platinating agents. *Cancer Treat. Rev.* **2007**, *33*, 9−23.

(8) (a) Johnstone, T. C.; Suntharalingam, K.; Lippard, S. J. Third row transition metals for the treatment of cancer. *Phil. Trans. R. Soc. A.* **2015**, *373*, 20140185. (b) Marloye, M.; Berger, G.; Gelbcke, M.; Dufrasne, F. A survey of the mechanisms of action of anticancer transition metal complexes. *Future Med. Chem.* **2016**, *8*, 2263−2286. (c) Odachowski, M.; Marschner, C.; Blom, B. A review on 1,1-bis(diphenylphosphino)methane bridged homo- and heterobimetallic complexes for anticancer applications: Synthesis, structure, and cytotoxicity. *Eur. J. Med. Chem.* **2020**, *204*, 112613. (d) Trédan, O.; Galmarini, C. M.; Patel, K.; Tannock, I. F. Drug resistance and the solid tumor microenvironment. *J. Natl. Cancer Inst.* **2007**, *99*, 1441−1454. (e) Hartinger, C. G.; Groessl, M.; Meier, S. M.; Casini, A.; Dyson, P. J. Application of mass spectrometric techniques to delineate the modes-of-action of anticancer metallodrugs. *Chem. Soc. Rev.* **2013**, *42*, 6186−6199.

(9) (a) Antonarakis, E. S.; Emadi, A. Ruthenium-based chemotherapeutics: are they ready for prime time? *Cancer Chemother. Pharmacol.* **2010**, *66*, 1−9. (b) Rademaker-Lakhai, J. M.; van den Bongard, D.; Pluim, D.; Beijnen, J. H.; Schellens, J. H. M. A phase I and pharmacological study with imidazolium-trans-DMSO-imidazole-tetrachlororuthenate, a novel ruthenium anticancer agent. *Clin. Cancer Res.* **2004**, *10*, 3717−3727. (c) Murray, B. S.; Babak, M. V.; Hartinger, C. G.; Dyson, P. J. The development of RAPTA compounds for the treatment of tumors. *Coord. Chem. Rev.* **2016**, *306*, 86−114. (d) Bergamo, A.; Gagliardi, R.; Scarcia, V.; Furlani, A.; Alessio, E.; Mestroni, G.; Sava, G. In vitro cell cycle arrest, in vivo action on solid metastasizing tumors, and host toxicity of the antimetastatic drug NAMI-A and cisplatin. *J. Pharmacol. Exp. Ther.* **1999**, *289*, 559−564. (e) Schluga, P.; Hartinger, C. G.; Egger, A.; Reisner, E.; Galanski, M.; Jakupec, M. A.; Keppler, B. K. Redox behavior of tumor-inhibiting ruthenium (III) complexes and effects of physiological reductants on their binding to GMP. *Dalton Trans.* **2006**, 1796−1802. (f) Lin, K.;

Zhao, Z.-Z.; Bo, H.-B.; Hao, X.-J.; Wang, J.-Q. Applications of Ruthenium Complex in Tumor Diagnosis and Therapy. *Front. Pharmacol.* **2018**, *9*, 1323. (g) Zeng, L.; Chen, Y.; Huang, H.; Wang, J.; Zhao, D.; Ji, L.; Chao, H. Cyclometalated ruthenium (II) anthraquinone complexes exhibit strong anticancer activity in hypoxic tumor cells. *Chem. – Eur. J.* **2015**, *21*, 15308−15319. (h) Allardyce, C. S.; Dyson, P. J.; Ellis, D. J.; Heath, S. L. [Ru(η^6-p-cymene)-Cl_2(pta)] (pta = 1,3,5-triaza-7-phosphatricyclo-[3.3.1.1]decane): A water soluble compound that exhibits pH dependent DNA binding providing selectivity for diseased cells. *Chem. Commun.* **2001**, *15*, 1396−1397. (i) Alessio, E.; Messori, L. NAMI-A and KP1019/1339, Two Iconic Ruthenium Anticancer Drug Candidates Face-to-Face: A Case Story in Medicinal Inorganic Chemistry. *Molecules* **2019**, *24*, 1995. (j) Tomšík, P.; Muthná, D.; Řezáčová, M.; Mičuda, S.; Ćmielová, J.; Hroch, M.; Endlicher, R.; Červinková, Z.; Rudolf, E.; Hann, S.; Stíbal, D.; Therrien, B.; Süss-Fink, G. [(p-$MeC_6H_4Pri)_2Ru_2(SC_6H_4$-p-But)$_3$]Cl (diruthenium-1), a dinuclear arene ruthenium compound with very high anticancer activity: An in vitro and in vivo study. *J. Organomet. Chem.* **2015**, *782*, 42−51. (k) Wu, B.; Ong, M. S.; Groessl, M.; Adhireksan, Z.; Hartinger, C. G.; Dyson, P. J.; Davey, C. A. A Ruthenium Antimetastasis Agent Forms Specific Histone Protein Adducts in the Nucleosome Core. *Chem. – Eur. J.* **2011**, *17*, 3562−3566. (l) Weiss, A.; Berndsen, R. H.; Dubois, M.; Müller, C.; Schibli, R.; Griffioen, A. W.; Dyson, P. J.; Nowak-Sliwinska, P. In vivo anti-tumor activity of the organometallic ruthenium(II)-arene complex [Ru(η^6-p-cymene)Cl_2(pta)] (RAPTA-C) in human ovarian and colorectal carcinomas. *Chem. Sci.* **2014**, *5*, 4742−4748.

(10) (a) Payne, R.; Govender, P.; Therrien, B.; Clavel, C. M.; Dyson, P. J.; Smith, G. S. Neutral and cationic multinuclear half-sandwich rhodium and iridium complexes coordinated to poly(propyleneimine) dendritic scaffolds: Synthesis and cytotoxicity. *Organomet. Chem.* **2013**, *729*, 20−27. (b) Liu, Z.; Sadler, P. J. Organoiridium complexes: anticancer agents and catalysts. *Acc. Chem. Res.* **2014**, *47*, 1174−1185. (c) Poth, T.; Paulus, H.; Elias, H.; Dücker-Benfer, C.; van Eldik, R. Kinetics and Mechanism of Water Substitution at Half-Sandwich Iridium (III) Aqua Cations Cp*Ir(A−B)$(H_2O)^{2+/+}$ in Aqueous Solution (Cp*= η^5-Pentamethylcyclopentadienyl Anion; A−B=Bi-dentate N,N or N,O Ligand). *Eur. J. Inorg. Chem.* **2001**, *2001*, 1361−1369.

(11) (a) Cattaruzza, L.; Fregona, D.; Mongiat, M.; Ronconi, L.; Fassina, A.; Colombatti, A.; Aldinucci, D. Antitumor activity of gold (III)-dithiocarbamato derivatives on prostate cancer cells and xenografts. *Int. J. Cancer* **2011**, *128*, 206−215. (b) Li, C. K. L.; Sun, R. W. Y.; Kui, S. C. F.; Zhu, N.; Che, C. M. Anticancer cyclometalated [AuIIIm(C∧N∧C)mL]n^+ compounds: synthesis and cytotoxic properties. *Chem. – Eur. J.* **2006**, *12*, 5253−5266. (c) Gabbiani, C.; Casini, A.; Messori, L.; Guerri, A.; Cinellu, M. A.; Minghetti, G.; Corsini, M.; Rosani, C.; Zanello, P.; Arca, M. Structural characterization, solution studies, and DFT calculations on a series of binuclear gold (III) oxo complexes: relationships to biological properties. *Inorg. Chem.* **2008**, *47*, 2368−2379. (d) Saggioro, D.; Rigobello, M. P.; Paloschi, L.; Folda, A.; Moggach, S. A.; Parsons, S.; Ronconi, L.; Fregona, D.; Bindoli, A. Gold (III)-dithiocarbamato complexes induce cancer cell death triggered by thioredoxin redox system inhibition and activation of ERK pathway. *Chem. Biol.* **2007**, *14*, 1128−1139. (e) Messori, L.; Abbate, F.; Marcon, G.; Orioli, P.; Fontani, M.; Mini, E.; Mazzei, T.; Carotti, S.; O'Connell, T.; Zanello, P. Gold (III) complexes as potential antitumor agents: solution chemistry and cytotoxic properties of some selected gold (III) compounds. *J. Med. Chem.* **2000**, *43*, 3541−3548. (f) Carotti, S.; Guerri, A.; Mazzei, T.; Messori, L.; Mini, E.; Orioli, P. Gold (III) compounds as potential antitumor agents: cytotoxicity and DNA binding properties of some selected polyamine-gold (III) complexes. *Inorg. Chim. Acta* **1998**, *281*, 90−94. (g) Zou, T.; Lum, C. T.; Lok, C.-N.; Zhang, J.-J.; Che, C.-M. Chemical biology of anticancer gold (III) and gold (I) complexes. *Chem. Soc. Rev.* **2015**, *44*, 8786−8801. (h) Bertrand, B.; Fernandez-Cestau, J.; Angulo, J.; Cominetti, M. M. D.; Waller, Z. A. E.; Searcey, M.; O'Connell, M. A.; Bochmann, M. Cytotoxicity of pyrazine-based cyclometalated (C^Npz^C) Au (III) carbene complexes: impact of the nature of the ancillary ligand on the biological properties. *Inorg. Chem.* **2017**, *56*, 5728−5740. (i) Mármol, I.; Castellnou, P.; Alvarez, R.; Gimeno, M. C.; Rodríguez-Yoldi, M. J.; Cerrada, E. Alkynyl Gold(I) complexes derived from 3-hydroxyflavones as multi-targeted drugs against colon cancer. *Eur. J. Med. Chem.* **2019**, *183*, 111661. (j) Estrada-Ortiz, N.; Lopez-Gonzales, E.; Woods, B.; Stürup, S.; de Graaf, I. A. M.; Groothuis, G. M. M.; Casini, A. Ex vivo toxicological evaluation of experimental anticancer gold(I) complexes with lansoprazole-type ligands. *Toxicol. Res.* **2019**, *8*, 885−895.

(12) (a) Nabiyeva, T.; Marschner, C.; Blom, B. Synthesis, structure and anti-cancer activity of osmium complexes bearing π-bound arene substituents and phosphane Co-Ligands: A review. *Eur. J. Med. Chem.* **2020**, *201*, 112483. (b) Maksimoska, J.; Williams, D. S.; Atilla-Gokcumen, G. E.; Smalley, K. S. M.; Carroll, P. J.; Webster, R. D.; Filippakopoulos, P.; Knapp, S.; Herlyn, M.; Meggers, E. Similar Biological Activities of Two Isostructural Ruthenium and Osmium Complexes. *Chem. – Eur. J.* **2008**, *14*, 4816−4822. (c) Schmid, W. F.; John, R. O.; Arion, V. B.; Jakupec, M. A.; Keppler, B. K. Highly Antiproliferative Ruthenium(II) and Osmium(II) Arene Complexes with Paullone-Derived Ligands. *Organometallics* **2007**, *26*, 6643−6652. (d) van Rijt, S. H.; Peacock, A. F. A.; Johnstone, R. D. L.; Parsons, S.; Sadler, P. J. Organometallic Osmium(II) Arene Anticancer Complexes Containing Picolinate Derivatives. *Inorg. Chem.* **2009**, *48*, 1753−1762. (e) Peacock, A. F. A.; Parsons, S.; Sadler, P. J. Tuning the Hydrolytic Aqueous Chemistry of Osmium Arene Complexes with N,O-Chelating Ligands to Achieve Cancer Cell Cytotoxicity. *J. Am. Chem. Soc.* **2007**, *129*, 3348−3357. (f) Dorcier, A.; Dyson, P. J.; Gossens, C.; Rothlisberger, U.; Scopelliti, R.; Tavernelli, I. Binding of Organometallic Ruthenium(II) and Osmium(II) Complexes to an Oligonucleotide: A Combined Mass Spectrometric and Theoretical Study. *Organometallics* **2005**, *24*, 2114−2123. (g) Dorcier, A.; Ang, W. H.; Bolaño, S.; Gonsalvi, L.; Juillerat-Jeannerat, L.; Laurenczy, G.; Peruzzini, M.; Phillips, A. D.; Zanobini, F.; Dyson, P. J. In Vitro Evaluation of Rhodium and Osmium RAPTA Analogues: The Case for Organometallic Anticancer Drugs Not Based on Ruthenium. *Organometallics* **2006**, *25*, 4090−4096.

(13) (a) Deacon-Price, C.; Romano, D.; Riedel, T.; Dyson, P. J.; Blom, B. Synthesis, characterisation and cytotoxicity studies of ruthenium arene complexes bearing trichlorogermyl ligands. *Inorg. Chim. Acta* **2019**, *484*, 513−520. (b) Berg, C.; Chari, S.; Jurgaityte, K.; Laurora, A.; Naldony, M.; Pope, F.; Romano, D.; Medupe, T.; Prince, S.; Ngubane, S.; Baumgartner, J.; Blom, B. Modulation of the solubility properties of arene ruthenium complexes bearing stannyl ligands as potential anti-cancer agents. *J. Organomet. Chem.* **2019**, *891*, 12−19.

(14) Aldeghi, N.; Romano, D.; Marschner, C.; Biswas, S.; Chakraborty, S.; Prince, S.; Ngubane, S.; Blom, B. Facile entry to germanate and stannate complexes [(η^6-arene)RuCl(η^2-dppm)]$^+$[ECl_3]$^-$ (E = Ge, Sn) as potent anti-cancer agents. *J. Organomet. Chem.* **2020**, *916*, 121214.

(15) Renier, O.; Deacon-Price, C.; Peters, J. E.; Nurekeyeva, K.; Russon, C.; Dyson, S.; Ngubane, S.; Baumgartner, J.; Dyson, P. J.; Riedel, T.; Chiririwa, H.; Blom, B. Synthesis and In Vitro (Anticancer) Evaluation of η^6-Arene Ruthenium Complexes Bearing Stannyl Ligands. *Inorganics* **2017**, *5*, 44.

(16) (a) Wang, H.; Yonker, N. J. D.; Gao, H.; Tan, C.; Zhang, X.; Ji, L.; Zhao, C.; Mao, Z.-W. Aquation and dimerization of osmium(II) anticancer complexes: a density functional theory study. *RSC Adv.* **2012**, *2*, 436−446. (b) Hanif, M.; Nazarov, A. A.; Hartinger, C. G.; Kandioller, W.; Jakupec, M. A.; Arion, V. B.; Dyson, P. J.; Keppler, B. K. Osmium(ii)−versus ruthenium(II)−arene carbohydrate-based anticancer compounds: similarities and differences. *Dalton Trans.* **2010**, *39*, 7345−7352.

(17) Hanif, M.; Babak, M. V.; Hartinger, C. G. Development of anticancer agents: wizardry with osmium. *Drug Discovery Today* **2014**, *19*, 1640−1648.

https://doi.org/10.1021/acsomega.1c02665
ACS Omega 2021, 6, 19252−19268

(18) van Rijt, S. H.; Hebden, A. J.; Amaresekera, T.; Deeth, R. J.; Clarkson, G. J.; Parsons, S.; McGowan, P. C.; Sadler, P. J. Amide linkage isomerism as an activity switch for organometallic osmium and ruthenium anticancer complexes. *J. Med. Chem.* **2009**, *52*, 7753−7764.
(19) (a) Nomura, A.; Tainaka, K.; Okamoto, A. Osmium complexation of mismatched DNA: effect of the bases adjacent to mismatched 5-methylcytosine. *Bioconjugate Chem.* **2009**, *20*, 603−607. (b) Zhang, P.; Huang, H. Future potential of osmium complexes as anticancer drug candidates, photosensitizers and organelle-targeted probes. *Dalton Trans.* **2018**, *47*, 14841−14854.
(20) Romero-Canelón, I.; Salassa, L.; Sadler, P. J. The Contrasting Activity of Iodido versus Chlorido Ruthenium and Osmium Arene Azo- and Imino-pyridine Anticancer Complexes: Control of Cell Selectivity, Cross-Resistance, p53 Dependence, and Apoptosis Pathway. *J. Med. Chem.* **2013**, *56*, 1291−1300.
(21) Nie, P.; Yu, Q.; Zhu, H.; Wen, T.-B. Ruthenium and Osmium Germyl Complexes Derived from the Reactions of $MXCl(PPh_3)_3$ (M = Ru, Os; X = Cl, H) with Terphenylchlorogermylene (C_6H_3-2,6-$Trip_2$)GeCl (Trip = 2,4,6-$^iPr_3C_6H_2$). *Eur. J. Inorg. Chem.* **2017**, *2017*, 4784−4796.
(22) Albertin, G.; Antoniutti, S.; Castro, J. Preparation of Half-Sandwich Stannyl Complexes of Osmium(II). *Organometallics* **2011**, *30*, 1914−1919.
(23) (a) Peacock, A. F. A.; Habtemariam, A.; Fernández, R.; Walland, V.; Fabbiani, F. P. A.; Parsons, S.; Aird, R. E.; Jodrell, D. I.; Sadler, P. J. Tuning the Reactivity of Osmium(II) and Ruthenium(II) Arene Complexes under Physiological Conditions. *J. Am. Chem. Soc.* **2006**, *128*, 1739−1748. (b) Castarlenas, R.; Esteruelas, M. A.; Oñate, E. N-Heterocyclic Carbene−Osmium Complexes for Olefin Metathesis Reactions. *Organometallics* **2005**, *24*, 4343−4346. (c) Werner, H.; Zenkert, K. Arene(phosphine) metal complexes. XIII. Osmium-(II) and osmium(0) complexes with p-cymene as the aromatic ligand. *J. Organomet. Chem.* **1988**, *345*, 151−166.
(24) Loos, M.; Gerber, C.; Corona, F.; Hollender, J.; Singer, H. Accelerated Isotope Fine Structure Calculation Using Pruned Transition Trees. *Anal. Chem.* **2015**, *87*, 5738−5744.
(25) (a) Mintmire, J. W.; Dunlap, B. I. Fitting the Coulomb potential variationally in linear-combination-of-atomic-orbitals density-functional calculations. *Phys. Rev. A* **1982**, *25*, 88−95. (b) Eichkorn, K.; Treutler, O.; Öhm, H.; Häser, M.; Ahlrichs, R. Auxiliary basis sets to approximate Coulomb potentials. *Chem. Phys. Lett.* **1995**, *240*, 283−290.
(26) Ahlrichs, R.; Bär, M.; Häser, M.; Horn, H.; Kölmel, C. Electronic structure calculations on workstation computers: The program system turbomole. *Chem. Phys. Lett.* **1989**, *162*, 165−169.
(27) Steffen, C.; Thomas, K.; Huniar, U.; Hellweg, A.; Rubner, O.; Schroer, A. TmoleX—A graphical user interface for TURBOMOLE. *J. Comput. Chem.* **2010**, *31*, 2967−2970.
(28) Weigend, F.; Ahlrichs, R. Balanced basis sets of split valence, triple zeta valence and quadruple zeta valence quality for H to Rn: Design and assessment of accuracy. *Phys. Chem. Chem. Phys.* **2005**, *7*, 3297−3305.
(29) (a) Hay, P. J.; Wadt, W. R. Ab initio effective core potentials for molecular calculations. Potentials for K to Au including the outermost core orbitals. *J. Chem. Phys.* **1985**, *82*, 299−310. (b) Wadt, W. R.; Hay, P. J. Ab initio effective core potentials for molecular calculations. Potentials for main group elements Na to Bi. *J. Chem. Phys.* **1985**, *82*, 284−298. (c) Hay, P. J.; Wadt, W. R. Ab initio effective core potentials for molecular calculations. Potentials for the transition metal atoms Sc to Hg. *J. Chem. Phys.* **1985**, *82*, 270−283.
(30) (a) Lee, C.; Yang, W.; Parr, R. G. Development of the Colle-Salvetti correlation-energy formula into a functional of the electron density. *Phys. Rev. B* **1988**, *37*, 785−789. (b) Becke, A. D., Density-functional thermochemistry. III. The role of exact exchange. *J. Chem. Phys.* **1993**, *98*, 5648−5652. (c) Becke, A. D. A new mixing of Hartree−Fock and local density-functional theories. *J. Chem. Phys.* **1993**, *98*, 1372−1377.
(31) (a) Mosmann, T. Rapid colorimetric assay for cellular growth and survival: Application to proliferation and cytotoxicity assays. *J. Immunol. Methods* **1983**, *65*, 55−63. (b) Verma, A. K.; Prasad, S. B. Changes in glutathione, oxidative stress and mitochondrial membrane potential in apoptosis involving the anticancer activity of cantharidin isolated from redheaded blister beetles, epicauta hirticornis. *Anti-Cancer Agents Med. Chem.* **2013**, *13*, 1096−1114.
(32) Bhattacharyya, M. K.; Saha, U.; Dutta, D.; Das, A.; Verma, A. K.; Frontera, A. Solvent-driven structural topology involving energetically significant intra- and intermolecular chelate ring contacts and anticancer activities of Cu(II) phenanthroline complexes involving benzoates: experimental and theoretical studies. *RSC Adv.* **2019**, *9*, 16339−16356.
(33) Zhang, H.; Holden-Wiltse, J.; Wang, J.; Liang, H. A Strategy to Model Nonmonotonic Dose-Response Curve and Estimate IC_{50}. *PLoS One* **2013**, *8*, No. e69301.
(34) (a) Squier, M. K. T.; Cohen, J. J. Standard quantitative assays for apoptosis. *Mol. Biotechnol.* **2001**, *19*, 305−312. (b) Prasad, S. B.; Verma, A. K. Cantharidin-Mediated Ultrastructural and Biochemical Changes in Mitochondria Lead to Apoptosis and Necrosis in Murine Dalton's Lymphoma. *Microsc. Microanal.* **2013**, *19*, 1377−1394.
(35) Atale, N.; Gupta, S.; Yadav, U. C. S.; Rani, V. Cell-death assessment by fluorescent and nonfluorescent cytosolic and nuclear staining techniques. *J. Microsc.* **2014**, *255*, 7−19.
(36) Chetry, S.; Sharma, P.; Frontera, A.; Dutta, D.; Verma, A. K.; Bhattacharyya, M. K. Unconventional formation of a 1D-chain of H-bonded water molecules in bipyridine-based supramolecular hexameric hosts of isostructural coordination compounds of Co(II) and Zn(II): Antiproliferative evaluation and theoretical studies. *Polyhedron* **2020**, *191*, 1−16.
(37) Daina, A.; Michielin, O.; Zoete, V. SwissADME: a free web tool to evaluate pharmacokinetics, drug-likeness and medicinal chemistry friendliness of small molecules. *Sci. Rep.* **2017**, *7*, 1−13.
(38) Michelin, R. A.; Mozzon, M.; Bertani, R. Reactions of transition metal-coordinated nitriles. *Coord. Chem. Rev.* **1996**, *147*, 299−338.
(39) Herry, B.; Batchelor, L. K.; Roufosse, B.; Romano, D.; Baumgartner, J.; Borzova, M.; Reifenstahl, T.; Collins, T.; Benamrane, A.; Weggelaar, J.; Correia, M. C.; Dyson, P. J.; Blom, B. Heterobimetallic Ru(μ-dppm)Fe and homobimetallic Ru(μ-dppm) Ru complexes as potential anti-cancer agents. *J. Organomet. Chem.* **2019**, *901*, 120934.
(40) (a) Pineda, L. W.; Jancik, V.; Roesky, H. W.; Neculai, D.; Neculai, A. M. Preparation and Structure of the First Germanium (II) Hydroxide: The Congener of an Unknown Low-Valent Carbon Analogue. *Angew. Chem., Int. Ed.* **2004**, *43*, 1419−1421. (b) Boyd, P. D. W.; Hart, M. C.; Pritzwald-Stegmann, J. R. F.; Roper, W. R.; Wright, L. J. Selective Substitution of One of the Substituents on Germanium in Coordinatively Unsaturated Ruthenium Germyl Complexes. *Organometallics* **2012**, *31*, 2914−2921.
(41) (a) Timm, M.; Saaby, L.; Moesby, L.; Hansen, E. W. Considerations regarding use of solvents in in vitro cell based assays. *Cytotechnology* **2013**, *65*, 887−894. (b) Peaston, A.; Maddison, J. Treatment of superficial tumours on horses with dimethyl sulfoxide and cisplatin. *Aust. Vet. J.* **1995**, *72*, 76−77.
(42) (a) Raghavan, R.; Cheriyamundath, S.; Madassery, J. Dimethyl sulfoxide inactivates the anticancer effect of cisplatin against human myelogenous leukemia cell lines in in vitro assays. *Indian J. Pharmacol.* **2015**, *47*, 322−324. (b) Hall, M. D.; Telma, K. A.; Chang, K.-E.; Lee, T. D.; Madigan, J. P.; Lloyd, J. R.; Goldlust, I. S.; Hoeschele, J. D.; Gottesman, M. M. Say no to DMSO: dimethylsulfoxide inactivates cisplatin, carboplatin, and other platinum complexes. *Cancer Res.* **2014**, *74*, 3913−3922. (c) Fischer, S. J.; Benson, L. M.; Fauq, A.; Naylor, S.; Windebank, A. J. Cisplatin and dimethyl sulfoxide react to form an adducted compound with reduced cytotoxicity and neurotoxicity. *NeuroToxicology* **2008**, *29*, 444−452. (d) Varbanov, H. P.; Ortiz, D.; Höfer, D.; Menin, L.; Galanski, M.; Keppler, B. K.; Dyson, P. J. Oxaliplatin reacts with DMSO only in the presence of water. *Dalton Trans.* **2017**, *46*, 8929−8932.

https://doi.org/10.1021/acsomega.1c02665
ACS Omega 2021, 6, 19252−19268

(43) Stockert, J. C.; Blázquez-Castro, A.; Cañete, M.; Horobin, R. W.; Villanueva, Á. MTT assay for cell viability: Intracellular localization of the formazan product is in lipid droplets. *Acta Histochem.* **2012**, *114*, 785−796.
(44) van Tonder, A.; Joubert, A. M.; Cromarty, A. Limitations of the 3-(4,5-dimethylthiazol-2-yl)-2,5-diphenyl-2H-tetrazolium bromide (MTT) assay when compared to three commonly used cell enumeration assays. *BMC Res. Notes* **2015**, *8*, 47.
(45) Taraphdar, A. K.; Roy, M.; Bhattacharya, R. K. Natural products as inducers of apoptosis: Implication for cancer therapy and prevention. *Curr. Sci.* **2001**, *80*, 1387−1396.
(46) Yamamoto, M.; Maehara, Y.; Oda, S.; Ichiyoshi, Y.; Kusumoto, T.; Sugimachi, K. The p53 tumor suppressor gene in anticancer agent-induced apoptosis and chemosensitivity of human gastrointestinal cancer cell lines. *Cancer Chemother. Pharmacol.* **1999**, *43*, 43−49.
(47) Xu, X.; Gao, X.; Jin, L.; Bhadury, P. S.; Yuan, K.; Hu, D.; Song, B.; Yang, S. Antiproliferation and cell apoptosis inducing bioactivities of constituents from Dysosma versipellis in PC3 and Bcap-37 cell lines. *Cell Div.* **2011**, *6*, 14.
(48) Lima, A. P.; Pereira, F. C.; Almeida, M. A. P.; Mello, F. M. S.; Pires, W. C.; Pinto, T. M.; Delella, F. K.; Felisbino, S. L.; Moreno, V.; Batista, A. A.; de Paula Silveira-Lacerda, E. Cytoxicity and Apoptotic Mechanism of Ruthenium(II) Amino Acid Complexes in Sarcoma-180 Tumor Cells. *PLoS One* **2014**, *9*, 105865.
(49) McConkey, B. J.; Sobolev, V.; Edelman, M. The performance of current methods in ligand−protein docking. *Curr. Sci.* **2002**, *83*, 845−856.
(50) Sathishkumar, N.; Sathiyamoorthy, S.; Ramya, M.; Yang, D.-U.; Lee, H. N.; Yang, D.-C. Molecular docking studies of anti-apoptotic BCL-2, BCL-XL, and MCL-1 proteins with ginsenosides from Panax ginseng. *J. Enzyme Inhib. Med. Chem.* **2012**, *27*, 685−692.

https://doi.org/10.1021/acsomega.1c02665
ACS Omega 2021, 6, 19252−19268